Cell Systems

Plausible, robust biological oscillations through allelic buffering

Graphical abstract

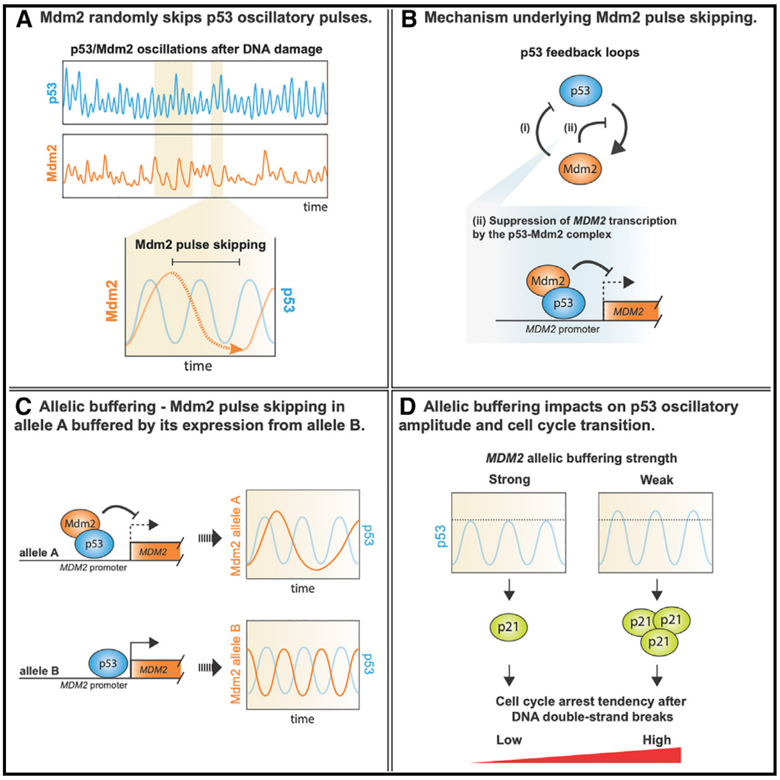

Highlights

- Allele-specific Mdm2 dynamics randomly skip p53 oscillatory pulses upon DNA damage
- Mdm2 pulse skipping is caused by a transcriptional inhibitory feedback loop of p53
- Allelic buffering among *MDM2* alleles maintains p53 amplitude for cell-cycle control
- Allelic buffering broadens the plausible biochemical space for oscillators to emerge

Authors

Feng-Shu Hsieh, Duy P.M. Nguyen, Mathias S. Heltberg, Chia-Chou Wu, Yi-Chen Lee, Mogens H. Jensen, Sheng-hong Chen

Correspondence

shengchen@gate.sinica.edu.tw

In brief

Using the p53 oscillator as a paradigm, Hsieh et al. investigate how biological oscillators achieve long-term oscillatory dynamics in the prevalence of biochemical noise. Combining quantitative live-cell imaging and stochastic modeling, they characterize the system-level mechanism underlying the robustness of sustained p53 oscillations. Their findings show that the p53 oscillator overcomes biochemical stochasticity through a de-noise mechanism—allelic buffering—which can facilitate the emergence of biological oscillators during evolution.

Hsieh et al., 2024, Cell Systems *15*, 1018–1032
November 20, 2024 © 2024 The Author(s). Published by Elsevier Inc.
https://doi.org/10.1016/j.cels.2024.10.002

CellPress
OPEN ACCESS

Cell Systems

Article

Plausible, robust biological oscillations through allelic buffering

Feng-Shu Hsieh,[1,4] Duy P.M. Nguyen,[1,4] Mathias S. Heltberg,[2,4] Chia-Chou Wu,[1,3,4] Yi-Chen Lee,[1] Mogens H. Jensen,[2] and Sheng-hong Chen[1,3,5,*]
[1]Lab for Cell Dynamics, Institute of Molecular Biology, Academia Sinica, Taipei 115, Taiwan
[2]Niels Bohr Institute, University of Copenhagen, Copenhagen 2100, Denmark
[3]National Center for Theoretical Sciences, Physics Division, Complex Systems, Taipei 10617, Taiwan
[4]These authors contributed equally
[5]Lead contact
*Correspondence: shengchen@gate.sinica.edu.tw
https://doi.org/10.1016/j.cels.2024.10.002

SUMMARY

Biological oscillators can specify time- and dose-dependent functions via dedicated control of their oscillatory dynamics. However, how biological oscillators, which recurrently activate noisy biochemical processes, achieve robust oscillations remains unclear. Here, we characterize the long-term oscillations of p53 and its negative feedback regulator Mdm2 in single cells after DNA damage. Whereas p53 oscillates regularly, Mdm2 from a single *MDM2* allele exhibits random unresponsiveness to ∼9% of p53 pulses. Using allelic-specific imaging of *MDM2* activity, we show that *MDM2* alleles buffer each other to maintain p53 pulse amplitude. Removal of *MDM2* allelic buffering cripples the robustness of p53 amplitude, thereby elevating p21 levels and cell-cycle arrest. *In silico* simulations support that allelic buffering enhances the robustness of biological oscillators and broadens their plausible biochemical space. Our findings show how allelic buffering ensures robust p53 oscillations, highlighting the potential importance of allelic buffering for the emergence of robust biological oscillators during evolution. A record of this paper's transparent peer review process is included in the supplemental information.

INTRODUCTION

Biological oscillations are widely observed in living organisms. For instance, circadian clocks govern daily physiological cycles, allowing better adaptation to day-to-night transitions. In response to injury or microbial infections, immune cells secrete cytokines (e.g., tumor necrosis factor alpha [TNF-α]) that activate and amplify inflammatory responses via oscillatory signaling.[1,2] At a molecular level, these biological oscillations usually arise from recurrent activation of sophisticated and stochastic biochemical reactions. For example, the signal-induced oscillations of transcription factors (TFs) usually involve activation of negative feedback loops,[1,3,4] in which gene transcription acts as a central mechanistic step. Gene transcription is intrinsically noisy due to the stochastic nature of TF binding to promoters.[5] Moreover, other biochemical processes, such as mRNA translation, can produce and amplify biochemical noise.[6,7] However, how biological oscillators overcome the stochasticity of biochemical reactions to achieve robust oscillations has remained largely elusive.

In response to DNA double-stranded breaks (DSBs), the tumor suppressor p53 elicits oscillatory dynamics that can be sustained for a long period of time.[8] Maintenance of these long-term p53 oscillations is critical to securing genome integrity by preventing cell-cycle re-entry in the presence of DNA damage[8] and safeguarding cells from premature senescence.[9] The p53-Mdm2 negative feedback loop is known to be a critical mechanism driving p53 oscillations.[10] As a transcriptional target of p53, Mdm2 ubiquitinates p53 for its proteasome-mediated degradation, hence forming a negative feedback loop. Similarly, other transcriptional targets of p53, such as Wip1, COP1, and Pirh2, have also been shown to form negative feedback loops of p53.[11–13] Given that gene transcription is intrinsically stochastic, variation in transcription of *MDM2* as well as other p53 negative feedback regulators is likely to occur during long-term oscillations of p53. Moreover, in addition to the transcriptional step, activation of p53 negative feedback loops involves a cascade of biochemical reactions (e.g., mRNA translation and protein ubiquitination) that can produce and amplify biological noise. It is unclear how long-term p53 oscillations, which require repetitive activation of its negative feedback loops, overcome biochemical noise to maintain its oscillatory dynamics.

In this study, we investigated the system-level mechanism underlying long-term robustness of p53 oscillations. Using live-cell imaging, we observed that though p53 oscillates regularly after DSBs, Mdm2 exhibits random allelic unresponsiveness to p53 pulses, herein termed "Mdm2 pulse skipping."

This phenomenon of Mdm2 pulse skipping is mainly driven by a p53 negative feedback loop that suppresses p53-mediated *MDM2* transcription. Using allele-specific imaging of *MDM2* activity, we show that *MDM2* alleles buffer each other during Mdm2 pulse skipping to specifically maintain a particular oscillatory dynamic feature of p53, i.e., pulse amplitude. Prolonged suppression of *MDM2* allelic buffering increased the mean and variation of p53 amplitude but not its pulse period duration, leading to a corresponding change in p21 expression and cellular state. Through mathematical modeling, we demonstrate that allelic buffering enhances the resistance of p53 oscillations to perturbations, thereby ultimately broadening the biochemical space for the emergence of robust p53 oscillators.

RESULTS

p53 oscillates with one period, but Mdm2 alternates between two oscillatory periods

To quantitatively characterize the long-term oscillations displayed by p53 and Mdm2, we engineered a multiplexed p53-Mdm2 reporter cell line, allowing us to simultaneously quantify p53 and Mdm2 protein levels in individual cells by fluorescence microscopy. Due to the dynamic nature of Mdm2 (i.e., its periodic transcription and short protein half-life),[14] we fused it to SYFP2, a fluorescent protein displaying strong brightness and a short maturation time.[15] Moreover, we examined and optimized the linkers (either short or long in length and flexible or rigid in structure, Figures S1A–S1C) between Mdm2 and SYFP2. Using a previously established MCF7 p53 reporter cell line,[16] we inserted a PA linker (six repeats of proline-alanine; Figure S1A) followed by SYFP2 at the C terminus of an endogenous human *MDM2* allele using CRISPR-Cas9 knockin technology (Figures S1D and S1E) and verified that the tagged Mdm2 protein preserves wild-type dynamics in response to DSBs (Figures S1F–S1I).

Using this p53-Mdm2 reporter cell line (Figures 1A and 1B), we quantified oscillatory dynamics of p53 and Mdm2 in individual cells after DNA damage over a period of 7.5 days (Figures 1C and 1D; Video S1). During this time window, each cell experienced ~40 pulses of p53, with an oscillatory period of 4.60 ± 0.44 h (mean ± standard deviation) (Figure 1E). The p53 oscillatory period is strongly robust over time, as revealed by the single dominant periodicity of the global wavelet spectrum (Figure 1F). By contrast, Mdm2 appeared to transition abruptly between two periods: one similar to that of p53 and another about twice as long (Figure 1G). These period transitions during Mdm2 oscillations are apparent from the bimodal distribution of Mdm2 period durations (Figure 1H), as opposed to the unimodal distribution of the p53 period (Figure 1F). The doubling of the Mdm2 period can also be seen from the Mdm2-to-p53 period ratio (Figure 1I), for which three time periods (60 to 90, 100 to 110, and 125 to 130 h in Figure 1I) show sharp step-wise increases from 1 to ~2. The occurrence of these distinct ~2-fold Mdm2-to-p53 period ratio transitions occupies 25% of the total p53 oscillatory period for the individual cell described in Figure 1J, and a mean of 22.3% across 406 cells (Figure S1J), implying the existence of a previously undescribed mode of Mdm2 oscillatory dynamics.

Mdm2 skips p53 pulses when it oscillates with a 2-fold longer period

To further investigate Mdm2 period transitions, we examined the single-cell dynamics of p53 and Mdm2 in detail. When the Mdm2-to-p53 period ratio changed to ~2 (Figure 2A; Video S2), we detected that Mdm2 levels became insensitive to p53 induction and consequently skipped a p53 pulse (Figure 2A, yellow shading). Hereafter, we refer to this unresponsiveness of Mdm2 to a p53 pulse as Mdm2 pulse skipping. Compared with the typical oscillations by which Mdm2 levels increase in response to each p53 induction, during Mdm2 pulse skipping, the Mdm2 level generally declines monotonically upon p53 induction (Figure 2A, yellow shading). Given this distinct Mdm2 behavior after p53 induction, Mdm2 pulse skipping exhibits opposing trajectories on the p53-Mdm2 phase plane compared with those of oscillatory Mdm2 (compare Figures 2B with 2C).

To determine if Mdm2 pulse skipping is a general phenomenon across a cell population, we plotted the oscillatory periods of p53 and Mdm2 at various time points for 406 cells. Although the majority of time points (72.7%) follow the diagonal trendline of a 1:1 Mdm2-to-p53 period ratio, notably a subset of time points (25.9%) clearly follows a steeper trendline of a 2:1 Mdm2-to-p53 period ratio, supporting the broad occurrence of Mdm2 pulse skipping (Figure 2D). To rigorously identify Mdm2 pulse skipping, we developed an algorithm to systematically search for a lack of Mdm2 induction between two p53 pulses using mathematically defined filters. To optimize the performance of the algorithm, an established ground truth dataset was used to adjust parameter values in the algorithm (see STAR Methods "Mdm2 pulse-skipping identification algorithm"; Figures S2A–S2C). The optimized algorithm enabled effective and automatic identification of Mdm2 pulse skipping (Figure S2D).

Mdm2 pulse skipping exhibits a prototypic dynamic feature and occurs randomly

We then explored if there is any prototypic dynamic feature of p53 and Mdm2 during Mdm2 pulse skipping. To do so, we aligned the dynamics of p53 and Mdm2 during oscillations and pulse-skipping events (Figure 2E). Interestingly, we observed that p53 does not seem to be greatly influenced by Mdm2 pulse-skipping events and shows similar periods and amplitudes (Figures 2E and 2F). By contrast, the pre-skip pulse of Mdm2 showed a pronounced increase in amplitude compared with that of an oscillatory one (Figures 2E and 2G), indicating a potential role for a higher Mdm2 level during the "pre-skip pulse" in eliciting subsequent Mdm2 pulse skipping. To determine if Mdm2 pulse skipping is a general phenomenon, we generated p53-Mdm2 reporter cells using A549 and RPE-1 cell lines that harbor different numbers of *MDM2* alleles. As shown in Figures S3A–S3C, MCF7, A549, and RPE-1 cells harbor four, three, and two copies of the *MDM2* allele, respectively. Furthermore, one *MDM2* allele was targeted for SYFP2 fusion in the MCF7 and RPE-1 cells, and two alleles were targeted for A549 cells (Figures S3D–S3F). In these two additional reporter cell lines (A549 and RPE-1), we also observed Mdm2 pulse skipping and the characteristic dynamic features of p53 and Mdm2 during these events (Figures S2E–S2I), supporting the general occurrence of Mdm2 pulse skipping across different human cell types,

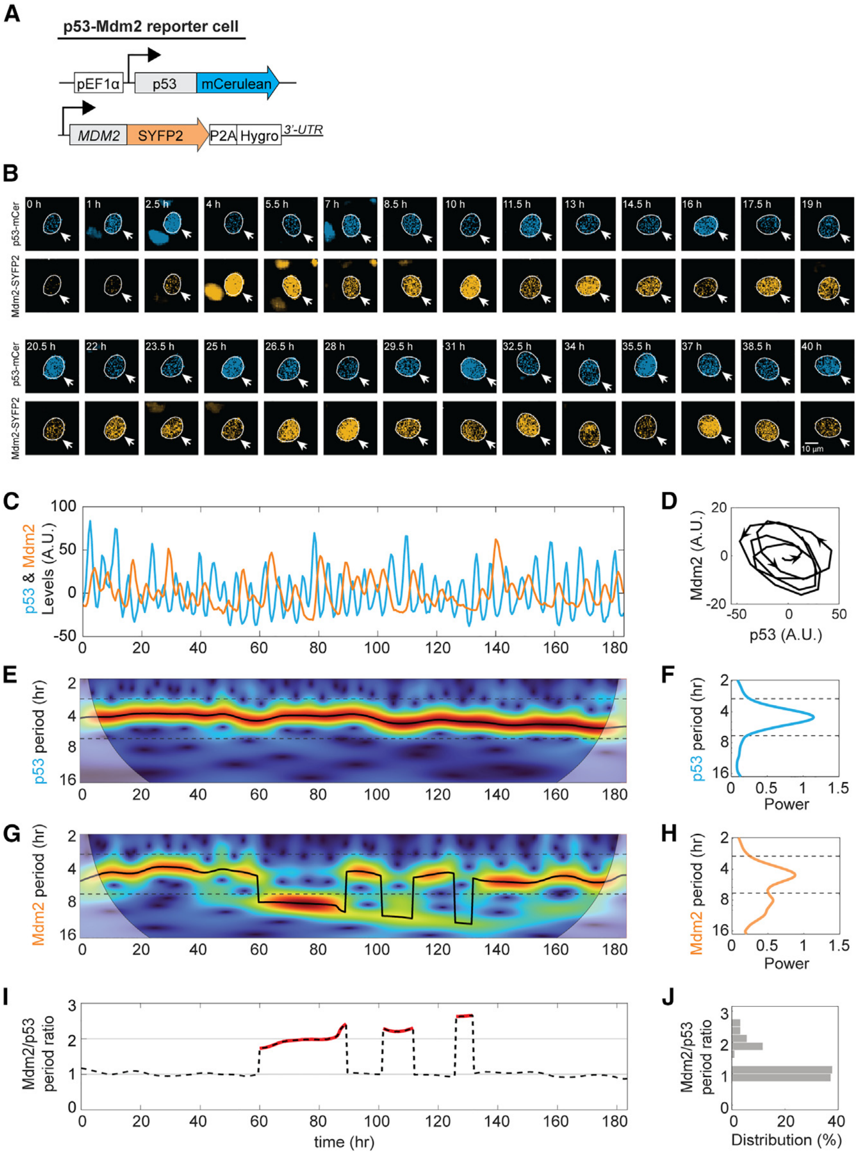

Figure 1. Mdm2 switches between two oscillatory periods, whereas p53 displays just one

(A) Schematic of the design of the p53-Mdm2 reporter cell line.

(B) Representative images of p53-mCerulean and Mdm2-SYFP2 at various time points following 400 ng/mL neocarzinostatin (NCS) treatment.

(C) Representative single-cell dynamics of p53 (blue) and Mdm2 (orange) following NCS treatment (400 ng/mL), quantified according to the fluorescence intensity of p53-mCerulean and Mdm2-SYFP2 in the nucleus.

(D) Phase diagram of the bandpass-filtered p53-Mdm2 trace in (C), from hours 5 and 25. Arrowheads indicate the direction of oscillations. The p53 and Mdm2 signals were smoothened with a time window of 1 h and subjected to third-degree polynomial filtering for detrending.

(E) Wavelet power spectrum of the p53 signal displayed in (C), ranging from minimum (blue) to maximum (red). The thick black line indicates the strongest period component.

(F) Global wavelet power spectrum of p53 derived from (E). Black dashed lines are 0.6 octaves away from the peak period component. The distribution of p53 period displays unimodality, $p > 0.05$, Cheng and Hall test.

(G) Wavelet power spectrum of the Mdm2 signal displayed in (C), ranging from minimum (blue) to maximum (red). The thick black line indicates the strongest period component.

(H) Global wavelet power spectrum of Mdm2 derived from (G). Black dashed lines are 0.6 octaves away from the peak period component. The distribution of Mdm2 period exhibits bimodality, $p < 0.05$, Cheng and Hall test.

(I) Mdm2-to-p53 period ratio over time. Durations of Mdm2 period > 0.6 octaves away from the peak p53 period component are marked in red.

(J) Histogram of the Mdm2-to-p53 period ratio for an individual cell from (I).

See also Figure S1.

regardless of the number of *MDM2* alleles. These results suggest a potentially shared underlying biochemical mechanism.

If Mdm2 pulse skipping is mainly driven by biochemical noise, its occurrence should be randomly distributed over time. To test that possibility, we quantified the time-dependent occurrence of Mdm2 pulse skipping. As shown in Figure 2H, pulse-skipping occurrence appears to be uniform over time, except for the more frequent occurrence of the second p53 pulse. Autocorrelation of pulse-skipping occurrence for individual cells revealed a drastic decrease after the first p53 pulse, further supporting the absence of a temporal pattern in Mdm2 pulse skipping (Figure S2J). If each Mdm2 pulse-skipping event occurs independently, then we would expect that the distribution of such events would follow a Poisson distribution. Indeed, the distribution of Mdm2 pulse skipping approximates a Poisson distribution, with a mean value of 0.091 per p53 pulse ($\lambda = 2.72$ per 30 p53 pulses), equivalent to a skipping event arising in 9.1% of p53 pulses (Figure 2I). Another indicator of the random nature of Mdm2 pulse skipping is the proximity of the distribution of intervals between two Mdm2 pulse-skipping events to an exponential function (mean $30/\lambda = 11.0$ p53 pulses) (Figure 2J). These results support that Mdm2 pulse skipping mostly occurs randomly over p53 oscillations at a constant rate.

Mdm2 pulse skipping is caused by suppression of *MDM2* transcription via the p53-Mdm2 inhibitory complex

Next, we sought to identify the potential mechanism by which Mdm2 pulse skipping occurs. As a negative regulator of p53, Mdm2 suppresses p53 through at least two negative feedback loops: (1) Mdm2 destabilizes p53 through ubiquitination-mediated proteasome degradation[17]; and (2) Mdm2 suppresses p53 transcriptional activity via formation of the p53-Mdm2 transcriptional inhibitory complex (Figure 3A).[18,19] Specifically, *MDM2* transcription can be suppressed by negative feedback

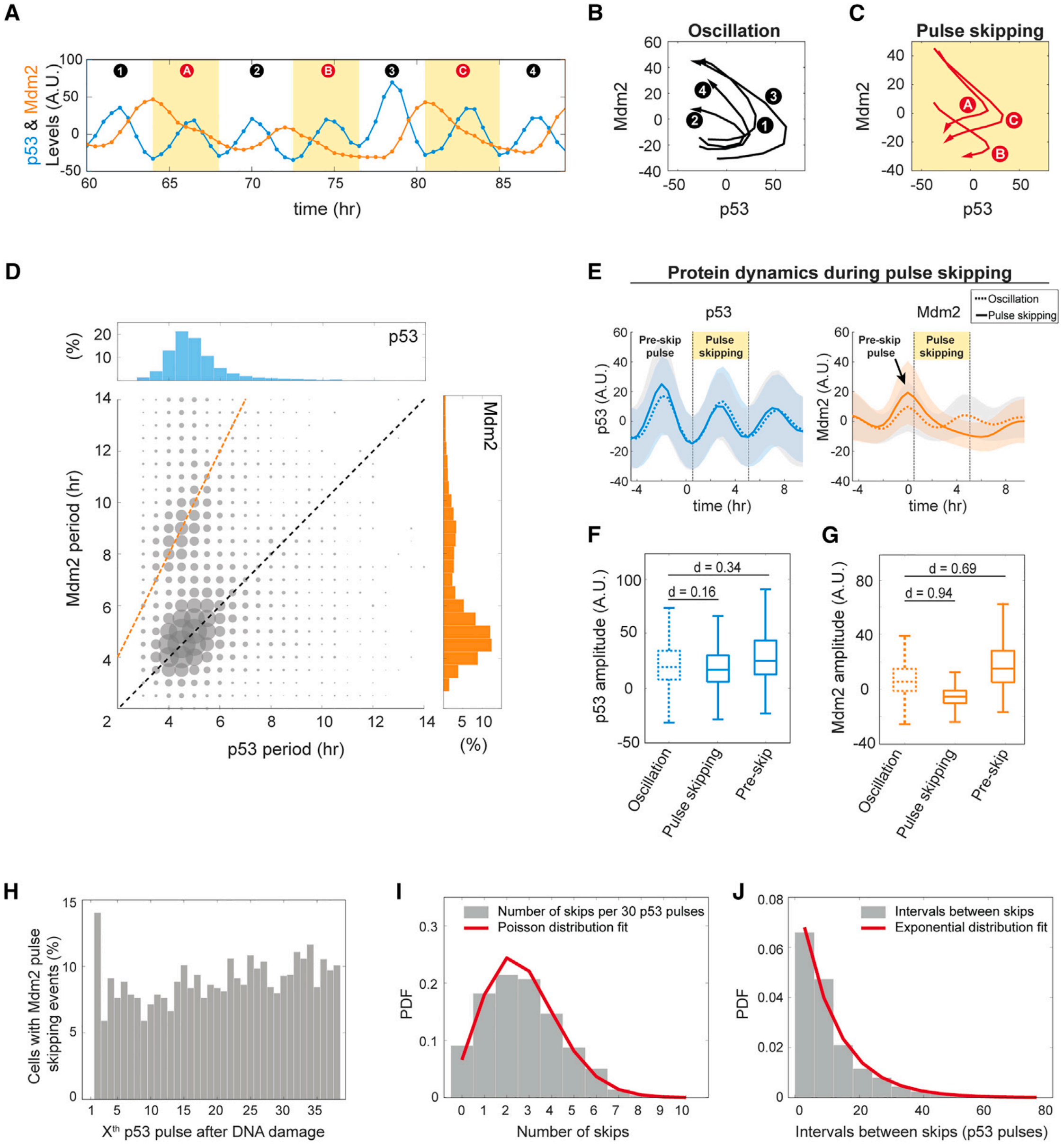

Figure 2. Mdm2 is unresponsive to p53 pulses when it oscillates with a 2-fold longer period

(A) Zoomed-in view of the time series in Figure 1C, from hours 60 to 89. Yellow-shaded areas highlight Mdm2 pulse-skipping events.

(B) Phase portrait of p53-Mdm2 signals during the oscillatory regime (60 to 64, 68 to 72.5, 76.5 to 80.5, and 85 to 89 h).

(C) Phase portrait of p53-Mdm2 signals during Mdm2 pulse-skipping events (64 to 68, 72.5 to 76.5, and 80.5 to 85 h).

(D) Bubble plot of p53 and Mdm2 periods (inter-peak interval). Bubble radius is proportional to sample size at each coordinate. Univariate histograms are shown above (p53) and to the right (Mdm2). The distribution of p53 period is unimodal ($p > 0.05$), while the distribution of Mdm2 period is bimodal ($p < 0.05$), Cheng and Hall test. Black dashed line is the 1:1 Mdm2-to-p53 period ratio. Orange dashed line is the 2:1 Mdm2-to-p53 period ratio.

(E) The dynamics of p53 (left) and Mdm2 (right) are aligned during Mdm2 pulse-skipping events (solid lines, $n = 1{,}133$) or oscillations (dashed lines, $n = 9{,}662$). Bold lines and shaded area represent mean and standard deviation, respectively. Black arrow indicates the higher amplitude of the Mdm2 pulse before the pulse-skipping event.

(F and G) Amplitude of p53 (F) and Mdm2 (G) pulses during or before Mdm2 pulse-skipping events ($n = 1{,}133$), compared with oscillatory pulses ($n = 9{,}662$). For all comparisons, $p < 0.05$, Wilcoxon rank sum test. Benchmarks for Cohen's d values for effect size: d = 0.2: a small mean difference; d = 0.5: a medium mean difference; and d = 0.8: a large mean difference.

(H) Histogram of the proportion of cells displaying Mdm2 pulse skipping over p53 pulses.

(I) Histogram of the number of Mdm2 pulse-skipping events per 30 p53 pulses. Fitted Poisson distribution in red. PDF, probability density function.

(J) Histogram of the intervals between Mdm2 pulse-skipping events. Fitted exponential distribution in red.

See also Figures S2 and S3.

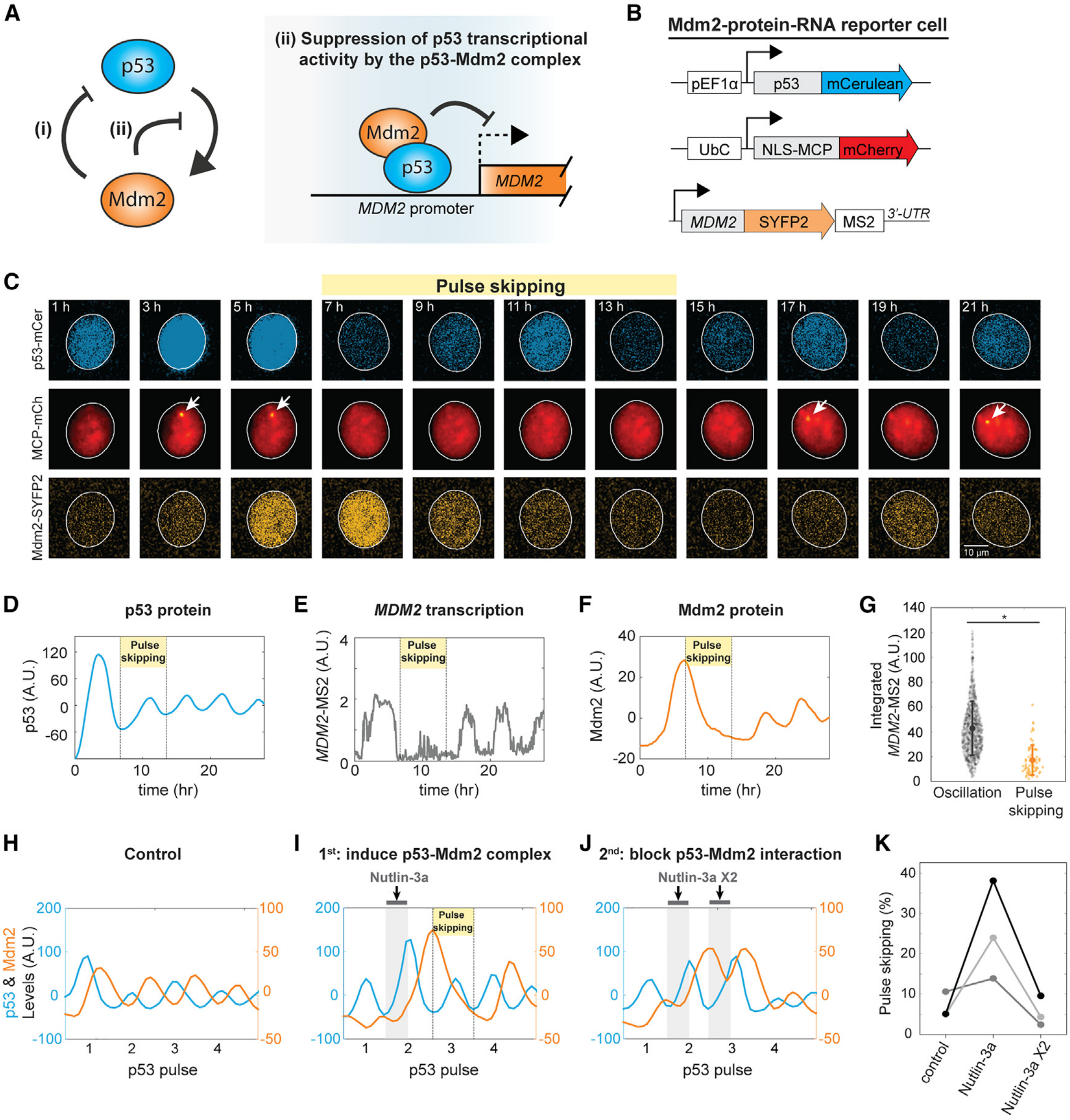

Figure 3. Mdm2 pulse skipping is attributable to compromised *MDM2* transcription via the p53-Mdm2 inhibitory complex

(A) Schematics of negative feedback loops (i) and (ii) of p53.

(B) Schematics of the design for the Mdm2-protein-RNA reporter cell line. p53 and Mdm2 proteins were fused to mCerelean and SYFP2, respectively. The endogenous *MDM2* allele was inserted with SYFP2, followed by MS2 stem loops.

(C) Representative images of p53-mCerulean, MCP-mCherry (*MDM2*-MS2 signal), and Mdm2-SYFP2 following 400 ng/mL neocarzinostatin (NCS) treatment. White arrows indicate the transcription foci. Yellow-shaded area indicates the occurrence of Mdm2 pulse skipping.

(D–F) Quantification of single-cell dynamics from (C): p53 protein (D), *MDM2* transcription (*MDM2*-MS2) (E), and Mdm2 protein (F).

(G) Integrated MS2 signal during Mdm2 pulse skipping ($n = 77$), compared with oscillations ($n = 812$). * represents $p < 10^{-27}$ by Wilcoxon rank sum test. A Cohen's d = 1.21 suggests a large mean difference. Each data point corresponds to one p53 pulse. Large dots and error bars indicate mean and standard deviation, respectively.

(H–J) Representative single-cell p53 and Mdm2 dynamics under different Nutlin-3a treatment schemes after NCS treatment. (H) A cell not treated with Nutlin-3a as control. (I) A cell treated with one phase of Nutlin-3a (3 μM for 2 h). (J) A cell treated with two phases of Nutlin-3a (first-phase: 3 μM for 2 h; second-phase: 0.75 μM for 2 h). Gray-shaded areas indicate the durations of Nutlin-3a treatments. Yellow-shaded areas represent the occurrence of Mdm2 pulse skipping.

(K) Mdm2 pulse skipping occurrence under different Nutlin-3a treatment schemes. Results from three independent experimental repeats are shown.

See also Figure S4.

loop (ii) as our chromatin immunoprecipitation (ChIP) assay revealed recruitment of both p53 and Mdm2 to the *MDM2* promoter (Figure S4A). Since the amplitude of pre-skip Mdm2 pulses tends to be higher (Figures 2E and 2G), we hypothesized that this higher level of Mdm2 enables transient formation of a higher level of Mdm2-p53 complex that suppresses subsequent

MDM2 transcription via negative feedback loop (ii) of Figure 3A, thereby eliciting an Mdm2 pulse-skipping event.

To test this hypothesis, first we assessed if Mdm2 pulse skipping is accompanied by a reduction in *MDM2* transcription. To this end, we developed an Mdm2-protein-RNA reporter cell line (Figures 3B, S4B, and S4C) that enabled us to simultaneously monitor *MDM2* transcription as well as Mdm2 and p53 protein levels by inserting MS2 stem loops in the 3′ untranslated region of the SYFP2-tagged *MDM2* allele. Consequently, upon active transcription of *MDM2*, MS2 stem loops would be bound by MS2 coat proteins fused to mCherry (MCP-mCherry), forming mCherry fluorescent foci on nascent RNAs at the transcription site (Figure 3C, middle panels). Each individual cell precisely shows one *MDM2* transcriptional focus when transcribed (Figure 3C; see also Figures S4D–S4F, the *MDM2*-MS2 foci are marked and correlated with *MDM2* single-molecule fluorescence *in situ* hybridization [smFISH] foci signals), indicating only one single *MDM2* allele was targeted in MCF7 cells (Table S1). Using this reporter cell line, we quantified the single-cell dynamics of p53 and Mdm2 proteins as well as *MDM2* transcription after DSBs (Figure 3C; Video S3). During the oscillatory regime, both *MDM2* transcription and Mdm2 protein levels oscillated with p53 levels (1 to 5 h and 15 to 21 h in Figures 3C and 3D–3F). By contrast, when Mdm2 pulse skipping occurred, we observed that *MDM2* transcription was greatly compromised (Figures 3C and 3D–3F, yellow shading; see Figure S4G for aligned dynamics across the cell population). As shown in Figure 3G, *MDM2*-MS2 signal was significantly lower during Mdm2 pulse skipping compared with that during oscillations across 370 cells, indicating a general weakening of *MDM2* transcription during Mdm2 pulse skipping.

Next, to investigate if the compromised *MDM2* transcription during pulse skipping is attributable to the p53-Mdm2 inhibitory complex, we quantitatively modulated its level using the small molecule Nutlin-3a. Nutlin-3a is a chemical that blocks the interaction between p53 and Mdm2,[20] thereby elevating p53 levels by suppressing its Mdm2-mediated ubiquitination. First, we conducted a first-phase Nutlin-3a (3 μM for 2 h) treatment during the rising phase of the second p53 pulse to transiently elevate the levels of both the second p53 and Mdm2 pulses, while preserving subsequent p53 oscillatory dynamics (Figure 3I). Here, maintenance of pulsatile p53 is critical to identifying subsequent pulse-skipping events. Our results indicate that this first-phase Nutlin-3a treatment indeed increased the levels of both p53 and Mdm2 and the occurrence of Mdm2 pulse skipping (Figure 3K; also compare Figures 3H with 3I). This increase in pulse-skipping events could be due to the elevated level of the p53-Mdm2 complex (Figures S4H and S4I).

To further examine the causality between p53-Mdm2 complex formation and the incidence of pulse skipping, we applied a second-phase Nutlin-3a (0.75 μM for 2 h) treatment during the rise of the third p53 pulse, when the elevated p53-Mdm2 complex was induced by the first-phase Nutlin-3a treatment (Figure 3J). Since Nutlin-3a can directly block the interaction between p53 and Mdm2, we expected that the p53-Mdm2 complex induced via first-phase Nutlin-3a treatment would be suppressed by the second-phase Nutlin-3a treatment. Indeed, we observed that the interaction between p53 and Mdm2 could be significantly suppressed by the second-phase Nutlin-3a treatment (Figures S4H and S4I). Furthermore, this second-phase Nutlin-3a treatment abolished the increase in Mdm2 pulse-skipping events induced by the first-phase Nutlin-3a treatment (Figure 3K; also compare Figure 3I with 3J), supporting the possibility that the formation of the p53-Mdm2 inhibitory complex promotes the occurrence of Mdm2 pulse skipping.

This proposed mechanism of negative feedback loop (ii) for Mdm2 pulse skipping is also consistent with the observation of a higher incidence of pulse-skipping events during the second pulse of p53 after DSBs (Figure 2H). After DSBs, the induced levels of p53 and Mdm2 in the first pulse are generally higher due to the immediate degradation of Mdm2 via DNA damage signaling.[14] The resulting higher level of the p53-Mdm2 inhibitory complex may then strengthen negative feedback loop (ii), resulting in a higher incidence of Mdm2 pulse-skipping events. Taken together, these results indicate that Mdm2 pulse skipping can be caused by suppression of *MDM2* transcription via the p53-Mdm2 inhibitory complex, i.e., p53 negative feedback loop (ii) depicted in Figure 3A.

p53 oscillatory amplitudes are maintained via allelic buffering during Mdm2 pulse skipping

Our observation of intact p53 oscillations during Mdm2 pulse-skipping challenges the widely accepted model of Mdm2 being the major negative regulator of the p53 oscillator and suggests the existence of a buffering mechanism. Since we monitored Mdm2 dynamics from a single *MDM2* allele in MCF7 cells (Figures 1, 2, 3, and, S3), the most parsimonious buffering effect can be attributed to the other three *MDM2* alleles. Specifically, during Mdm2 pulse skipping of one allele (upper panel, Figure 4A), the remaining alleles can contribute to the production of Mdm2, allowing p53 degradation via ubiquitination-driven negative feedback loop (i) (lower panel, Figure 4A). To experimentally test this allelic buffering mechanism, we developed an *MDM2* dual-allele reporter cell line (Figures 4B and S5A–S5E) to simultaneously monitor p53 dynamics as well as the activities of two *MDM2* alleles: one based on its RNA transcription via the MS2 stem-loop signal and the other based on its protein translation through the SYFP2 fusion signal (Table S1). The MS2 stem-loop system was utilized for its timely responsiveness to dynamic changes in *MDM2* transcriptional activity.[21]

Using this *MDM2* dual-allele reporter cell line, we observed that Mdm2 pulse skipping could occur in either *MDM2* allele or both, resulting in the following four scenarios: no pulse skipping (83.7% of p53 pulses); only *MDM2* transcription-related pulse skipping (8.6% of p53 pulses); only Mdm2 protein-related pulse skipping (6.6% of p53 pulses); or pulse skipping of both alleles (1.2% of p53 pulses) (Figure 4C for single-cell traces; Figures S5F–S5H for representative images; Figure S5I for aligned dynamics over a cell population; see also Videos S4, S5, and S6). In particular, after pulse skipping of only one *MDM2* allele (i.e., either transcription- or protein-related pulse-skipping events), the amplitude of post-skip p53 remained similar to that of p53 pulses with no skipping (Figure 4D). By contrast, after double-allele skipping events, the subsequent post-skip p53 amplitude was significantly higher (Figure 4D, red line), indicating a transient weakening of allelic buffering. In comparison, the prototypic higher amplitude of pre-skip Mdm2 occurred in both single-allele and double-allele pulse-skipping

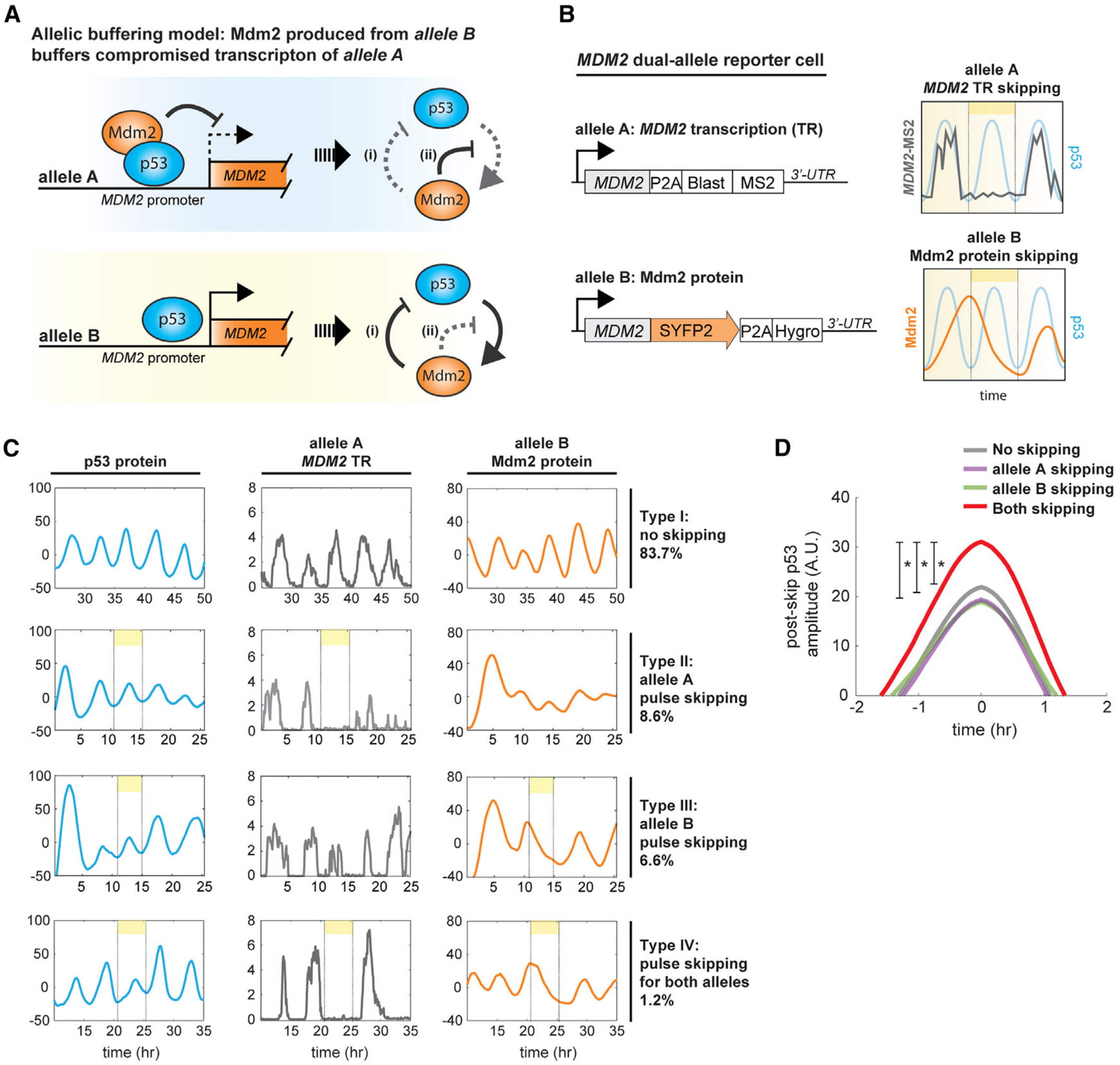

Figure 4. Allelic buffering maintains p53 oscillatory amplitudes during Mdm2 pulse skipping

(A) Schematics of the allelic buffering model.

(B) Schematics of the design of the *MDM2* dual-allele reporter cells. Endogenous *MDM2* alleles were fused with either MS2 stem loops (allele A, upper left) or SYFP2 (allele B, lower left). Engineered allele A allows characterization of *MDM2* transcriptional pulse skipping (upper right), whereas engineered allele B enables characterization of Mdm2 protein pulse skipping (lower right).

(C) Representative single-cell dynamics of p53 protein, *MDM2* transcription (*MDM2*-MS2) from allele A, and Mdm2 protein from allele B. Yellow-shaded areas mark the occurrence of Mdm2 pulse skipping.

(D) Mean level of p53 pulses after Mdm2 pulse skipping for either or both alleles (allele A pulse skipping: $n = 157$, allele B pulse skipping: $n = 120$, pulse skipping for both alleles: $n = 22$), compared with that of oscillations ($n = 1{,}533$). * represents $p < 0.05$ by Wilcoxon rank sum test. A Cohen's d > 0.6 suggests a medium to large mean difference.

See also Figure S5.

events (Figure S5J), a dynamic feature not observed for p53 (Figure S5K). In summary, our experimental results support the existence of allelic buffering during Mdm2 pulse skipping and its function in maintaining p53 amplitude during oscillations.

In silico simulations support the maintenance of robust p53 oscillatory amplitude via allelic buffering

To further quantitatively investigate how allelic buffering might impact p53 oscillations, we developed a simplified mathematical model incorporating both negative feedback loops (Figure 3A) to simulate p53 oscillatory dynamics under the regulation of two *MDM2* alleles (A and B in Figure 5A; see also STAR Methods "mathematical modeling and stochastic simulations" and Table S2). Our simulations of Mdm2 pulse skipping exhibit a similar frequency (Figures 5B, S6H, and S6I) and dynamic features (Figures 5C and S6A–S6G) with our experimental results. Using this model, we investigated *in silico* how sustained loss of allelic buffering might affect p53 dynamics (Figures 5C–5F). We observed that p53 oscillatory period was not altered after sustained transcriptional suppression of one *MDM2* allele

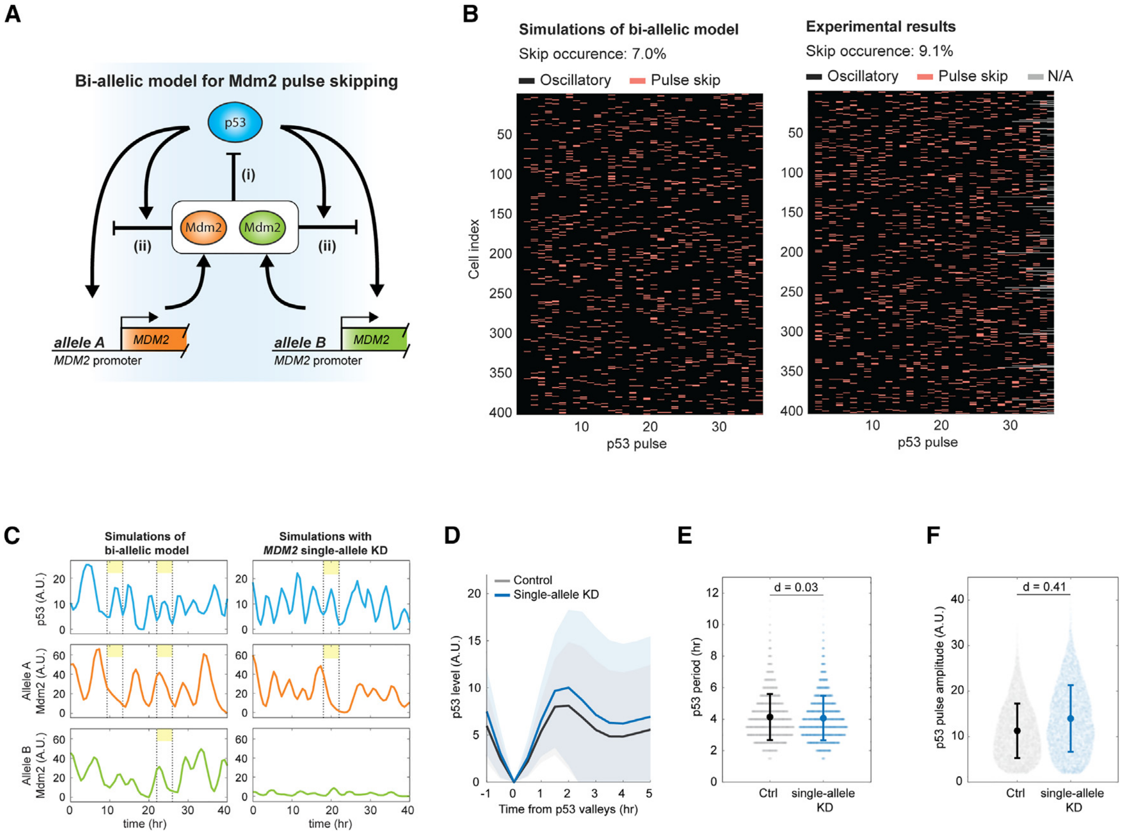

Figure 5. ***In silico* simulations reveal the function of allelic buffering in maintaining robust p53 oscillatory amplitude**

(A) Schematics of the bi-allelic model for Mdm2 pulse skipping. (i) and (ii) represent the two negative feedback loops of p53 (see Figure 3A).

(B) Temporal occurrence of Mdm2 pulse skipping events in single cells from *in silico* simulations of the bi-allelic model (left, 7.0%) or experimental data (right, 9.1%). N/A, p53 peak not available.

(C) Simulations of the single-cell dynamics of p53 and Mdm2 from the bi-allelic model without (left) or with *MDM2* single-allele knockdown (KD, right). Yellow-shaded areas represent the occurrence of Mdm2 protein skipping. *MDM2* single-allele KD was achieved by enhancing the degradation of *MDM2* mRNA from allele B.

(D) Aligned p53 dynamics of simulated control (n = 16,533) compared with *MDM2* single-allele knockdown (n = 16,732). The time series were subtracted and aligned according to preceding p53 valleys. Mean (solid line) and standard deviation (shading) are shown.

(E) Distribution of p53 period (inter-peak interval, IPI) in simulated control (Ctrl) (n = 16,533) compared with *MDM2* single-allele knockdown (n = 16,732). Each data point corresponds to one IPI. Dot and error bars indicate mean and standard deviation, respectively. p = 0.0538, Wilcoxon rank sum test. A Cohen's d = 0.03 suggests a small mean difference.

(F) Distribution of p53 pulse amplitude in simulated control (Ctrl) (n = 16,533) compared with *MDM2* single-allele knockdown (n = 16,732). Each data point corresponds to one p53 pulse. Dot and error bars indicate mean and standard deviation, respectively. $p < 10^{-250}$, Wilcoxon rank sum test. A Cohen's d = 0.41 suggests a small to medium mean difference.

See also Figure S6.

(Figures 5D and 5E). By contrast, the amplitude of p53 pulses was significantly altered, displaying a higher mean value (Figures 5D and 5F). These simulation results imply a major influence of allelic buffering on p53 oscillatory amplitude.

p53 oscillatory amplitude encodes information for cell-cycle control

To experimentally test the amplitude-specific impact of allelic buffering, we knocked down one allele of *MDM2* using allele-specific small interfering RNAs (siRNAs) (see STAR Methods "siRNA knockdown"). As shown in the middle panel of Figure 6A, p53 retained its oscillations following single-allele *MDM2* knockdown. By contrast, *MDM2* all-allele knockdown greatly disrupted p53 oscillations, evidencing an essential role for Mdm2 in maintaining p53 oscillations (right panel, Figure 6A; see dynamics in cell populations in Figures S7A–S7C). After single-allele *MDM2* knockdown, we detected a higher (+22.4% in mean value) p53 amplitude compared with that of the control (Figures 6B and 6D). By contrast, there was no detectable change in p53 period upon single-allele *MDM2* knockdown (Figure 6C), indicating an amplitude-specific modulation via allelic buffering. Together, both our simulation and experimental results reveal a role for *MDM2* allelic buffering in maintaining p53 amplitude.

The amplitude-specific effect of allelic buffering allowed us to further investigate the biological function encoded in p53 oscillatory amplitude. Specifically, we wondered if changes in p53 amplitude (Figure 6D) can be sensed by cells via the expression

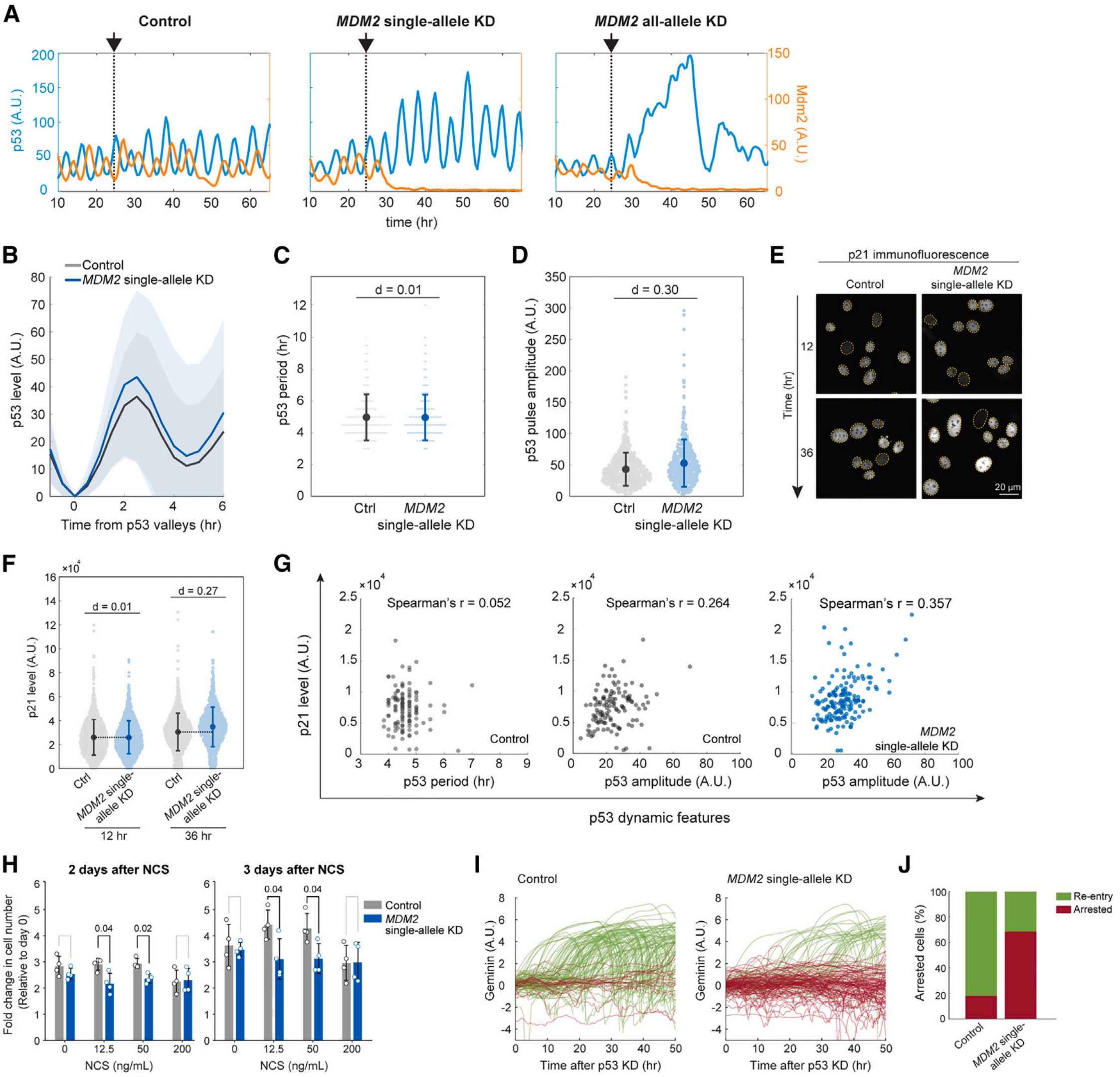

Figure 6. Allelic buffering maintains the robustness of p53 oscillatory amplitude, which encodes information for cell-cycle control

(A) Representative single-cell p53 (blue) and Mdm2 (orange) dynamics after transfection of scrambled siRNAs (left, control), *MDM2* allele-specific siRNAs (middle, single-allele KD), or *MDM2* general siRNAs (right, all-allele KD). Knockdown was performed 24 h after NCS (400 ng/mL) treatment, indicated by black arrows.

(B) Aligned p53 dynamics after control knockdown ($n = 709$), compared with *MDM2* single-allele knockdown ($n = 585$). Time series were subtracted and aligned according to preceding p53 valleys. Mean (solid line) and standard deviation (shading) are shown.

(C) Distribution of p53 period (IPI) after control knockdown ($n = 709$) compared with *MDM2* single-allele knockdown ($n = 585$). Each data point corresponds to one IPI. Dot and error bars indicate mean and standard deviation, respectively. $p = 0.8327$, Wilcoxon rank sum test. A Cohen's d = 0.01 indicates a small mean difference.

(D) Distribution of p53 pulse amplitude after control knockdown ($n = 709$) compared with *MDM2* single-allele knockdown ($n = 585$). Each data point corresponds to one p53 pulse. Large dot and error bars indicate mean and standard deviation, respectively. $p < 10^{-6}$, Wilcoxon rank sum test. A Cohen's d = 0.30 indicates a small to medium difference.

(E and F) Representative images of p21 immunofluorescence (E) and the distribution of p21 protein nuclear intensity (F) 12 and 36 h after control ($n = 1{,}353$ and 1,331) or *MDM2* single-allele knockdown ($n = 1{,}439$ and 1,124). Knockdown was performed 24 h after 400 ng/mL NCS treatment. Each data point corresponds to one cell nucleus. Large dot and error bars indicate mean and standard deviation, respectively. A Cohen's d = 0.01 suggests a small mean difference; d = 0.27 suggests a small to medium mean difference.

(G) Correlation between p21 immunofluorescence and p53 dynamic features, i.e., p53 period (IPI) and p53 amplitude. Dynamic features of p53 were extracted from the time series 20–36 h after control ($n = 122$) or *MDM2* single-allele knockdown ($n = 156$). p21 levels were quantified using immunofluorescence 36 h after knockdown. Each dot represents quantifications from one cell. The Spearman's correlation coefficient is shown above each panel.

(H) The proliferation of cell populations with or without *MDM2* allele-specific knockdown at the indicated time after low doses of NCS treatment. Fold-change in cell number normalized to that of day 0 is presented. Mean and standard deviation (error bar) from four technical repeats (empty circle) are shown. An identical pattern of fold-change differences was observed from three independent experimental repeats. Statistical significance was determined by performing a Wilcoxon rank sum test. p values below 0.05 are shown.

(legend continued on next page)

of p53 downstream targets, such as p21. Previous studies have shown that p21 can be sensitive to changes in p53 amplitude.[22,23] Consistently, when we knocked down one allele of *MDM2*, we observed an increase in p21 protein level (Figures 6E and 6F). This p21 elevation was only apparent 36 h after *MDM2* single-allele knockdown, coinciding with the knockdown kinetics of *MDM2* (Figures 6F and S7D). To further examine which dynamic feature of p53 encodes the information for p21 induction, we conducted a correlation analysis between p21 levels and p53 dynamic features (Figures 6G and S7E). p53 amplitude exhibited a much stronger correlation with p21 compared with p53 period (Figure 6G). The correlation between p21 and p53 amplitude was further enhanced by *MDM2* single-allele knockdown (right panel, Figure 6G), underscoring the importance of p53 oscillatory amplitude in regulating p21 levels.

As a regulator of cell-cycle progression, high levels of p21 can lead to cell-cycle arrest after DNA damage.[24] Accordingly, we wondered if p21 suppression via allelic buffering promotes the cell-cycle transition in response to DNA damage. To test this possibility, we first examined if allelic buffering promotes cell-cycle progression when cells experience low levels of DNA damage. As shown in Figure 6H, cells with intact allelic buffering proliferate faster than those with reduced allelic buffering (via *MDM2* single-allele knockdown). Second, we explored if arrested cells with intact allelic buffering are more likely to re-enter the cell cycle. To do so, we knocked down p53 in cells experiencing high-level DSBs. Using Geminin induction as an indicator of cell-cycle re-entry, we observed that a cell population with weaker allelic buffering showed a higher percentage (68.7%) of arrested cells compared with that (18%) of control cells (Figures 6I and 6J; see Figure S7F for the extent of p53 knockdown), indicating that cell-cycle re-entry is promoted via allelic buffering. Collectively, these results support the possibility that *MDM2* allelic buffering suppresses p21 levels via modulation of p53 oscillatory amplitude, which fine-tunes the population-level tendency for cell-cycle progression during DNA damage.

MDM2 allelic buffering strengthens the robustness of p53 oscillations and broadly expands the oscillatory regime

The above-described results inspired us to further investigate *in silico* if allelic buffering generally strengthens the robustness of the p53 oscillator. To do so, we examined how p53 oscillatory features (i.e., amplitude and period) respond to systematic perturbations (0.5- to 2-fold perturbations) of the individual biochemical mechanism represented by each parameter in our mathematical model (see STAR Methods "sensitivity analysis"). Exploring the biochemical space closely matching the p53 oscillator in human cells, our simulations revealed that p53 oscillations are generally more resistant to perturbations in the two-allele model compared with those in the one-allele model (Figures 7A and S8A), highlighting the importance of allelic buffering in maintaining robust p53 oscillations.

Functional encoding of p53 oscillations is not limited to amplitude but also period. Recently, the maintenance of p53 oscillatory period within an appropriate range was proposed to be critical for efficient DNA damage repair.[25] Accordingly, we explored if *MDM2* allelic buffering exerts a general role in maintaining functional p53 oscillations. Here, the functional p53 oscillatory regime is defined according to physiological levels of p53 oscillatory period and amplitude. We then explored *in silico* the plausible biochemical space for a functional p53 oscillator. As shown in Figures 7B and 7C, the biochemical space for a functional p53 oscillator is 3.9-fold larger in a two-allele model compared with that in a one-allele model. For example, when the transcription rate of *MDM2* is 15-fold smaller and *MDM2* mRNA translation is 63-fold larger than their original values, p53 can still exhibit functional oscillations in a two-allele model but not in a one-allele model (Figure S8B). In conclusion, these results indicate that *MDM2* allelic buffering enhances the resistance of the p53 oscillator to biochemical noise and broadens the biochemical space for a functional p53 oscillator to emerge during the course of evolution.

DISCUSSION

In the face of pervasive biochemical noise, signaling systems need to develop de-noise strategies to robustly maintain their dynamics in order to precisely elicit cellular functions in space and time. In particular, an oscillatory system undergoes recurrent activation of complex biochemical reactions that can be especially vulnerable to noise production and amplification. In this study, using the p53 oscillator as an appropriate paradigm, we demonstrate that biochemical noise causes stochastic formation of a high-level p53-Mdm2 inhibitory complex that suppresses allelic *MDM2* transcription, resulting in Mdm2 pulse skipping. However, through allelic buffering from the other *MDM2* alleles, p53 maintains its oscillatory amplitude during Mdm2 pulse-skipping events. Such allelic buffering can potentially play a general role in facilitating the robustness and emergence of biological oscillators.

The random occurrence of Mdm2 pulse skipping (Figures 2H–2J) implies its origin from biochemical noise. During activation of the two p53 negative feedback loops (Figure 3A), multiple biochemical reactions can generate and amplify biochemical noise. Gene transcription is known to be generally stochastic due to low gene copy numbers.[26] In the case of the p53 oscillator, *MDM2* transcription can be an intrinsically stochastic process. This transcriptional noise can be further exacerbated by the p53 negative feedback loop (ii) (Figure 3A), whereby the p53-Mdm2 inhibitory complex binds to the *MDM2* promoter to suppress *MDM2* transcription. Formation of this p53-Mdm2 inhibitory complex is also likely to be noisy as it integrates

---

(I) Single-cell dynamics of geminin after p53 knockdown in cells with (n = 134) or without (control, n = 122) *MDM2* allele-specific knockdown. p53 knockdown was performed 36 h after *MDM2* allelic knockdown, and cell entry into S phase was tracked by geminin induction. Single-cell geminin traces indicate either cell-cycle re-entry (elevated geminin levels: entry into S phase, green) or G1 phase cell-cycle arrest (red) 50 h after p53 knockdown.

(J) Percentage of arrested (red) versus cell-cycle re-entry cells (green) 50 h after p53 knockdown from cells subjected to control (n = 122) or *MDM2* single-allele knockdown (n = 134).

See also Figure S7.

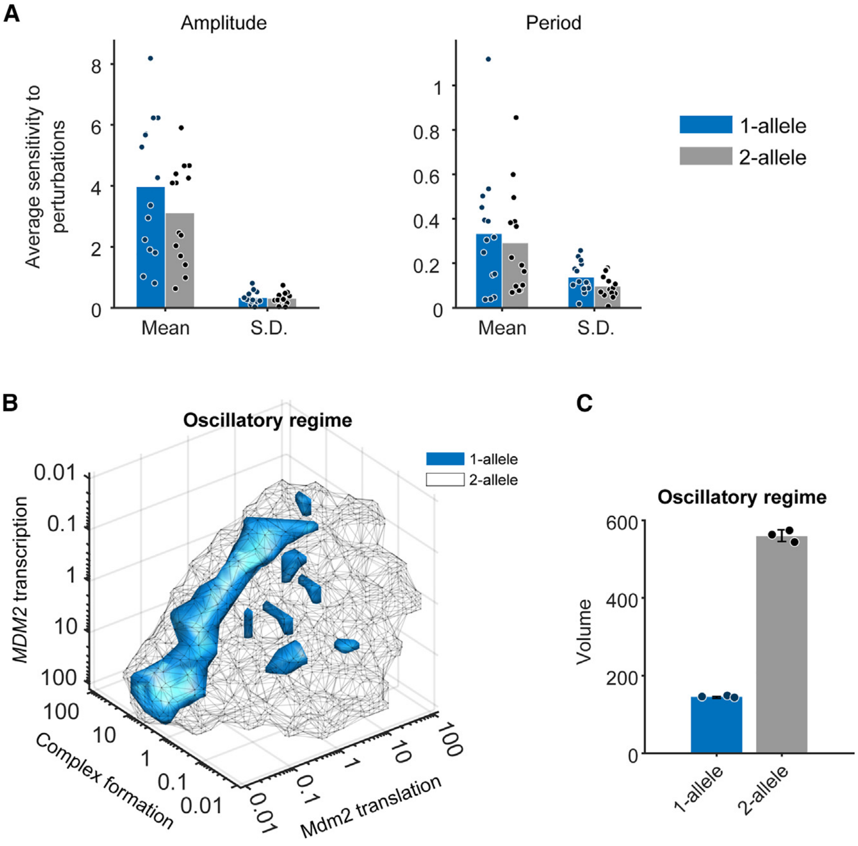

Figure 7. Allelic buffering strengthens the robustness of p53 oscillations and broadens its oscillatory regime

(A) Average sensitivity of mean and standard deviation (SD) of the p53 amplitude and period to perturbations in the two-allele model compared with the one-allele model. Averages of the sensitivity coefficients over the 14 parameters are shown. Each dot represents the sensitivity coefficient of an individual parameter (see Figure S8A).

(B) The p53 oscillatory regimes in the two-allele model compared with the one-allele model. The oscillatory regimes are defined as having at least 98% of simulations with (i) p53 oscillatory amplitude within two standard deviations above and below the physiological mean and (ii) p53 period between 3 and 7 h (see STAR Methods "construction of the p53 oscillatory regime"). Parameters were perturbed by 0.01- to 100-fold of their original values (see Table S2). For each combination of the three perturbed parameters, 500 simulations were analyzed. See also Figure S8C for the oscillatory regimes from two additional independent repeats.

(C) The volume of p53 oscillatory regimes in the two-allele model compared with that of the one-allele model from three independent batches of 500 simulations. Mean and standard deviation (error bar) are shown.

See also Figure S8.

biochemical noise arising from the production and degradation of p53 and Mdm2. Therefore, the stochastic occurrence of Mdm2 pulse skipping can be attributed to biochemical noise from both *MDM2* transcription and formation of the p53-Mdm2 inhibitory complex. Furthermore, the occurrence of Mdm2 pulse-skipping events is not governed by a deterministic threshold of Mdm2 amplitude in the pre-skip pulse (Figure S2K). Instead, a higher pre-skip Mdm2 amplitude simply increases the likelihood of an Mdm2 pulse-skipping event during the next p53 pulse (Figure S2L), supporting the stochastic nature of Mdm2 pulse skipping.

Biochemically, the p53-Mdm2 inhibitory complex competes with transcriptionally active p53 oligomers for binding to the *MDM2* promoter. Thus, their relative abundances and/or binding affinities to the *MDM2* promoter determine the relative strength of the two negative feedback loops (Figure 3A) and, consequently, the frequency of Mdm2 pulse-skipping events. We anticipate the frequency of Mdm2 pulse skipping to be higher when p53-Mdm2 complexes occupy the *MDM2* promoter for a longer period of time compared with that of the p53 oligomers. It is possible that different organisms may have evolved differential frequencies of Mdm2 pulse skipping by modulating this biochemical process, e.g., altering the binding affinity between the p53-Mdm2 inhibitory complex and the *MDM2* promoter via mutations in the binding site. Increasing the frequency of Mdm2 pulse-skipping events may elicit more high-amplitude p53 pulses after double-allele pulse-skipping events (Figure 4D), representing a dynamic feature that enhances the tendency for cell-cycle arrest and cellular senescence upon genotoxic stress.

This biochemical antagonism between the p53-Mdm2 inhibitory complex and p53 oligomers can occur not only at the *MDM2* gene but also at other downstream target genes of p53. A recent study indicated that *CDKN1A*, the gene encoding p21, displays a pulse-skipping frequency of ∼3% during p53 oscillations.[27] This lower pulse-skipping frequency in *CDKN1A* can be caused by a weaker affinity of the p53-Mdm2 inhibitory complex for the gene promoter compared with that of p53 oligomers, resulting in overall higher transcriptional activity during p53 oscillations. Therefore, through the evolution of the promoter binding affinity of the p53-Mdm2 inhibitory complex, oscillatory p53 can elicit different pulse-skipping frequencies in its downstream targets, allowing for diversification in gene expression. At a global scale, p53 oscillatory dynamics have been shown to facilitate greater diversity in gene expression profiles compared with sustained p53.[28],[29] The biochemical antagonism between the p53-Mdm2 inhibitory complex and p53 oligomers provides an additional mechanistic explanation for how oscillatory p53 generates diverse expression of downstream targets and ensures gene-specific transcriptional activities. We envision that genes with a higher frequency of pulse skipping will exhibit weaker expression levels when normalized to integrated p53 levels. In addition to the p53 oscillator, signal-induced oscillations of TFs (e.g., nuclear factor κB [NF-κB]) elicit gene-specific transcriptional activities, and it would be interesting to investigate the involvement of this biochemical antagonism in diversifying gene transcription in other oscillatory TFs.

Despite harboring different *MDM2* copy numbers (Figures S3A–S3C), all three cell lines we tested exhibit Mdm2 pulse skipping with similar prototypic Mdm2 dynamics (Figures S2E–S2I). To quantitatively investigate the effect of varying numbers of *MDM2* alleles *in silico*, we expanded our mathematical model to include up to six *MDM2* alleles. Consistent with experimental results, our simulations revealed several key findings supporting the general occurrence of Mdm2 pulse skipping and the functional significance of allelic buffering. First, increasing the number of *MDM2* alleles leads to an increase in the frequency of Mdm2 pulse-skipping events (Figure S9C), indicating a higher buffering capacity toward pulse skipping. Consistently, there is a decrease in the Mdm2 pulse-skipping frequency from 9% to 4.3% following *MDM2* single-allele knockdown (Figure S9D). Note that the increase in *MDM2* alleles does not disrupt p53 oscillations but leads to a mild and monotonic decrease in both the period and amplitude of p53 oscillations, which can be attributed to the increase in the inhibitory effect of Mdm2 (Figures S9A and S9B). Second, an increase in the number of *MDM2* alleles further strengthens the robustness of the p53 oscillator against perturbations (Figures S9E and S9F) and increases its oscillatory regime (Figure S9G). These results support the general notion that *MDM2* allelic buffering, a property enhanced by increasing the number of *MDM2* alleles, promotes the robustness and emergence of the p53 oscillator.

In addition to Mdm2, p53 has other negative feedback regulators (e.g., Mdmx, Wip1, COP1, and Pirh2) that play a critical role in controlling p53-mediated stress responses.[11–13,23] Although it is known that Mdm2, Mdmx, and Wip1 regulate p53 oscillatory dynamics,[10,30,31] the mechanism by which other negative regulators modulate p53 oscillations remains unclear. Given their identical feedback loop topology, we suspect that these negative feedback regulators could also help maintain robust p53 oscillations by buffering biochemical noise. If this is the case, suppression of these negative feedback regulators would compromise the overall buffering capacity and robustness of p53 oscillations. To test this hypothesis, we conducted simulations in the presence or absence of Q, a Mdm2-independent negative feedback regulator, and examined the resulting p53 and Mdm2 oscillations. Similar to the effects of decreasing *MDM2* alleles, absence of Q caused less robust p53 oscillations (Figure S10A) and a reduction in Mdm2 pulse-skipping events (Figure S10B). Therefore, inclusion of an Mdm2-independent negative feedback regulator can help enhance buffering capacity for robust p53 oscillations and permits a higher frequency of Mdm2 pulse skipping. Interestingly, p53 negative feedback regulators can exert quantitatively distinct effects on p53 oscillations. Whereas *MDM2* knockdown greatly disrupts p53 oscillatory dynamics (right panel, Figures 6A and S7C), Wip1 suppression alters the steady state, shape, and uniformity of p53 oscillations.[30] It will be important to quantitatively characterize the functional role of individual negative feedback regulators, particularly their contribution to the robustness of p53 oscillations and tissue-specific oscillatory dynamics.[32]

Biochemical stochasticity can be decomposed into intrinsic versus extrinsic noise.[33,34] Intrinsic noise refers to the inherent stochasticity from the system of interest, whereas extrinsic noise comes indirectly from global fluctuations outside of the system. Our observation of allele-specific Mdm2 pulse skipping (Figure 4C, type II and type III) prompted us to further interrogate the respective roles of extrinsic and intrinsic noise in governing Mdm2 pulse skipping. In the case of *MDM2* transcription, extrinsic noise would exert a global effect on all *MDM2* alleles within the same nucleus, whereas intrinsic noise would cause allele-specific variation in transcriptional activity. To examine the presence of extrinsic noise during single-allele pulse skipping, we quantified the expression of the non-skipping allele during single-allele pulse skipping. As shown in Figure S11, when a single-allele pulse-skipping event occurs, the expression level of the other non-skipping allele is also greatly compromised (single-cell examples in Figure S11A; quantifications in cell populations in Figures S11B–S11D) compared with that of oscillatory conditions, indicating global transcriptional suppression in all *MDM2* alleles during single-allele pulse skipping. Therefore, the occurrence of Mdm2 pulse skipping can be partly governed by extrinsic noise. This extrinsic noise could be mediated by the shared and diffusive p53-Mdm2 inhibitory complex in negative feedback loop (ii) (Figure 3A).

Certainly, there is stronger transcriptional suppression for the skipped *MDM2* allele compared with the non-skipped one during single-allele pulse skipping. This allele-specific transcriptional suppression that lasts for up to 2–3 h during p53 pulses can be attributed to intrinsic noise. Similarly, this allele-specific transcriptional suppression was previously observed to last more than 10 h.[35] However, the mechanism underlying this intrinsic noise remains unclear. For the p53 oscillator, we suspect that the prolonged transcriptional suppression of a single *MDM2* allele could be due to stochastic formation of transcriptionally inhibitory Mdm2 oligomers.[19] It is known that Mdm2 can transition between monomeric and oligomeric states of more than 10 subunits.[36] Since the activity of the upstream kinase that regulates this monomer-to-oligomer transition is highly dynamic after DNA damage,[30] it is tempting to speculate that Mdm2 oligomer formation is stochastic. Once an Mdm2 oligomer has formed locally at a particular *MDM2* allele, its interactions with p53 and the *MDM2* promoter can be especially tight via its oligomer-mediated multivalent interactions, leading to prolonged allele-specific transcriptional suppression. We hope that our proposed model can inspire future investigations into the mechanism underlying allele-specific intrinsic noise, which represents an important yet unanswered question in the field.

At the organismal level, *MDM2* haplo-insufficiency has been shown to enhance p53-dependent sensitivity to ionizing radiation.[37,38] In our study, when we specifically silenced one *MDM2* allele, thereby mimicking *MDM2* haplo-insufficiency in human cells, we detected an apparent increase in the mean p53 oscillatory amplitude (Figures 6B and 6D), but not its period (Figure 6C). This amplitude-specific change in p53 results in a corresponding elevation in p21 levels and a significant shift in cellular tendency to remain in cell-cycle arrest (Figures 6H–6J). We suspect that, in addition to p53 amplitude-mediated p21 induction, this strong shift in cellular state can be attributed to other mechanisms, including effects from other p53 target genes[39,40] and/or Mdm2-dependent regulation of the G1-S transition.[41] Since cells that remain in cell-cycle arrest are more likely to undergo senescence, our results may provide a system-level understanding for why *MDM2* haplo-insufficient animals are hypersensitive to ionizing radiation. Given the ubiquitous nature of oscillatory TFs[42,43] and the preponderance of human pathologies attributable to haplo-insufficiency,[44] a comprehensive assessment of the significance of allelic buffering in human pathologies is now warranted.

Maintaining robust biological oscillations is critical for cells and organisms to precisely exert functions in space and time.[45] Previous studies have demonstrated the emergence of biological oscillators with robust amplitudes but tunable periods via the coupling of positive and negative feedback loops.[46] Moreover, linking two negative feedback loops enhances the entrainment capacity of biological oscillators, enabling a robust cellular response to external signals.[47,48] Here, we show, both experimentally and through *in silico* simulations, that allelic buffering enables robust and precise control over p53 oscillatory amplitude, a dynamic feature for cell-cycle control. Although numerous theories have been proposed for how biological oscillators emerge during the course of evolution,[31,46,49,50] few consider the maintenance of both robust oscillatory amplitudes and periods for functional biological oscillators. We demonstrate the criticality of allelic buffering for the robust control of these dynamic features that can facilitate the emergence of biological oscillators during evolution. In the future, it will be interesting to explore the role of allelic buffering in different existing biological oscillators and how it may contribute to the behavior and design of synthetic biological oscillators.

RESOURCE AVAILABILITY

Lead contact

Further information and requests for resources and reagents should be directed to and will be fulfilled by the lead contact, Sheng-hong Chen (shengchen@gate.sinica.edu.tw).

Materials availability

Materials generated for this study will be made available upon request to the lead contact.

Data and code availability

- Single-cell data have been deposited at Zenodo (https://doi.org/10.5281/zenodo.13743894) and are publicly available as of the date of publication. Due to the limitations in repository size, microscopy data reported in this paper will be shared by the lead contact upon request.
- All original code has been deposited at Zenodo and is publicly available as of the date of publication. DOIs are listed in the key resource table.
- Any additional information required to reanalyze the data reported in this paper is available from the lead contact upon request.

ACKNOWLEDGMENTS

We thank members of the Lab for Cell Dynamics, especially Hannah K.C. Co, for helpful discussions and suggestions. We are grateful to Su-Ping Lee at the Imaging Core and Shu-Yun Tung at the Genomics Core of the Institute of Molecular Biology for their technical assistance. We appreciate Jun-An Chen and Kuan-Wei Chen for their help with the chromatin immunoprecipitation assay and the assistance from the Core Facilities of Academia Sinica (AS-CFII-113-A12 and AS-CFII-111-212). This work was supported by the Academia Sinica Career Development Award Grant (AS-CDA-108-L01), the Academia Sinica Grand Challenge Program Seed Grant (AS-GCS-111-L04), the National Taiwan University and Academia Sinica Innovative Joint Program (AS-NTU-112-04), and the National Science and Technology Council Grant (112-2311-B-001-025 and 113-2311-B-001-027). M.S.H. and M.H.J. acknowledge the support from the Independent Research Fund Denmark (9040-00116B), the Novo Nordisk Foundation (NNF20OC0064978), and the Lundbeck Foundation (R347-2020-2250).

AUTHOR CONTRIBUTIONS

F.-S.H., D.P.M.N., and S.-h.C. conceived and designed the project. F.-S.H. and S.-h.C. designed the experiments. F.-S.H. carried out the experiments with help from Y.-C.L. F.-S.H., D.P.M.N., and C.-C.W. analyzed the experimental data with inputs from all authors. D.P.M.N. developed the Mdm2 pulse-skipping detection algorithm with inputs from M.S.H. and S.-h.C. D.P.M.N. initiated and C.-C.W. optimized the bi-allelic mathematical model with guidance from M.S.H. and S.-h.C. D.P.M.N., M.S.H., and C.-C.W. contributed to simulations. M.S.H. and M.H.J. provided expertise on oscillatory systems. F.-S.H. and S.-h.C. wrote the manuscript with inputs from all authors. S.-h.C. supervised the project and acquired the financial support to conduct the project.

DECLARATION OF INTERESTS

The authors declare no competing interests.

STAR★METHODS

Detailed methods are provided in the online version of this paper and include the following:

- KEY RESOURCES TABLE
- EXPERIMENTAL MODEL AND SUBJECT DETAILS
  - ○ Cell culture
  - ○ Gene targeting and reporter cell development
- METHOD DETAILS
  - ○ siRNA knockdown
  - ○ Plasmids and cloning
  - ○ Imaging-based assessment of Mdm2-linker-SYFP2 localization and stability
  - ○ DNA Fluorescence In Situ Hybridization (DNA FISH)
  - ○ Quantitative PCR for determining gene copy number
  - ○ Immunoblotting
  - ○ Immunofluorescence
  - ○ Live-cell microscopy
  - ○ Proximity ligation assay (PLA)
  - ○ Chromatin Immunoprecipitation and quantitative real-time PCR (ChIP-qPCR)
  - ○ Single-molecule FISH
  - ○ Single-cell tracking
- QUANTIFICATION AND STATISTICAL ANALYSIS
  - ○ Quantification of single-cell p53-Mdm2 protein dynamics
  - ○ Quantification of p53 and Mdm2 oscillatory periods
  - ○ Mdm2 pulse skipping identification algorithm
  - ○ Examining the occurrence of Mdm2 pulse skipping as a random process
  - ○ Quantification of *MDM2* transcriptional intensity
  - ○ Mathematical modeling and stochastic simulations
  - ○ Implementation of the Gillespie algorithm
  - ○ Detection of Geminin induction
  - ○ Sensitivity analysis
  - ○ Construction of the p53 oscillatory regime
  - ○ The half-life of the autocorrelation
  - ○ Statistical analysis

SUPPLEMENTAL INFORMATION

Supplemental information can be found online at https://doi.org/10.1016/j.cels.2024.10.002.

Received: December 30, 2023
Revised: August 12, 2024
Accepted: October 10, 2024
Published: November 5, 2024

REFERENCES

1. Hoffmann, A., Levchenko, A., Scott, M.L., and Baltimore, D. (2002). The IkappaB-NF-kappaB signaling module: temporal control and selective gene activation. Science *298*, 1241–1245. https://doi.org/10.1126/science.1071914.
2. Tay, S., Hughey, J.J., Lee, T.K., Lipniacki, T., Quake, S.R., and Covert, M.W. (2010). Single-cell NF-kappaB dynamics reveal digital activation and analogue information processing. Nature *466*, 267–271. https://doi.org/10.1038/nature09145.
3. Lev Bar-Or, R., Maya, R., Segel, L.A., Alon, U., Levine, A.J., and Oren, M. (2000). Generation of oscillations by the p53-Mdm2 feedback loop: a theoretical and experimental study. Proc. Natl. Acad. Sci. USA *97*, 11250–11255. https://doi.org/10.1073/pnas.210171597.
4. Hirata, H., Yoshiura, S., Ohtsuka, T., Bessho, Y., Harada, T., Yoshikawa, K., and Kageyama, R. (2002). Oscillatory expression of the bHLH factor Hes1 regulated by a negative feedback loop. Science *298*, 840–843. https://doi.org/10.1126/science.1074560.
5. Raj, A., and van Oudenaarden, A. (2008). Nature, nurture, or chance: stochastic gene expression and its consequences. Cell *135*, 216–226. https://doi.org/10.1016/j.cell.2008.09.050.
6. Ozbudak, E.M., Thattai, M., Kurtser, I., Grossman, A.D., and van Oudenaarden, A. (2002). Regulation of noise in the expression of a single gene. Nat. Genet. *31*, 69–73. https://doi.org/10.1038/ng869.
7. Thattai, M., and van Oudenaarden, A. (2001). Intrinsic noise in gene regulatory networks. Proc. Natl. Acad. Sci. USA *98*, 8614–8619. https://doi.org/10.1073/pnas.151588598.
8. Reyes, J., Chen, J.Y., Stewart-Ornstein, J., Karhohs, K.W., Mock, C.S., and Lahav, G. (2018). Fluctuations in p53 Signaling Allow Escape from Cell-Cycle Arrest. Mol. Cell *71*, 581–591.e5. https://doi.org/10.1016/j.molcel.2018.06.031.
9. Purvis, J.E., Karhohs, K.W., Mock, C., Batchelor, E., Loewer, A., and Lahav, G. (2012). p53 dynamics control cell fate. Science *336*, 1440–1444. https://doi.org/10.1126/science.1218351.
10. Geva-Zatorsky, N., Rosenfeld, N., Itzkovitz, S., Milo, R., Sigal, A., Dekel, E., Yarnitzky, T., Liron, Y., Polak, P., Lahav, G., and Alon, U. (2006). Oscillations and variability in the p53 system. Mol. Syst. Biol. *2*, 2006.0033. https://doi.org/10.1038/msb4100068.
11. Lu, X., Ma, O., Nguyen, T.A., Jones, S.N., Oren, M., and Donehower, L.A. (2007). The Wip1 Phosphatase acts as a gatekeeper in the p53-Mdm2 autoregulatory loop. Cancer Cell *12*, 342–354. https://doi.org/10.1016/j.ccr.2007.08.033.
12. Dornan, D., Wertz, I., Shimizu, H., Arnott, D., Frantz, G.D., Dowd, P., O’Rourke, K., Koeppen, H., and Dixit, V.M. (2004). The ubiquitin ligase COP1 is a critical negative regulator of p53. Nature *429*, 86–92. https://doi.org/10.1038/nature02514.
13. Leng, R.P., Lin, Y., Ma, W., Wu, H., Lemmers, B., Chung, S., Parant, J.M., Lozano, G., Hakem, R., and Benchimol, S. (2003). Pirh2, a p53-induced ubiquitin-protein ligase, promotes p53 degradation. Cell *112*, 779–791. https://doi.org/10.1016/s0092-8674(03)00193-4.
14. Stommel, J.M., and Wahl, G.M. (2004). Accelerated MDM2 auto-degradation induced by DNA-damage kinases is required for p53 activation. EMBO J. *23*, 1547–1556. https://doi.org/10.1038/sj.emboj.7600145.
15. Kremers, G.J., Goedhart, J., van Munster, E.B., and Gadella, T.W., Jr. (2006). Cyan and yellow super fluorescent proteins with improved brightness, protein folding, and FRET Forster radius. Biochemistry *45*, 6570–6580. https://doi.org/10.1021/bi0516273.
16. Gaglia, G., Guan, Y., Shah, J.V., and Lahav, G. (2013). Activation and control of p53 tetramerization in individual living cells. Proc. Natl. Acad. Sci. USA *110*, 15497–15501. https://doi.org/10.1073/pnas.1311126110.
17. Haupt, Y., Maya, R., Kazaz, A., and Oren, M. (1997). Mdm2 promotes the rapid degradation of p53. Nature *387*, 296–299. https://doi.org/10.1038/387296a0.
18. Momand, J., Zambetti, G.P., Olson, D.C., George, D., and Levine, A.J. (1992). The mdm-2 oncogene product forms a complex with the p53 protein and inhibits p53-mediated transactivation. Cell *69*, 1237–1245. https://doi.org/10.1016/0092-8674(92)90644-r.
19. Nomura, K., Klejnot, M., Kowalczyk, D., Hock, A.K., Sibbet, G.J., Vousden, K.H., and Huang, D.T. (2017). Structural analysis of MDM2 RING separates degradation from regulation of p53 transcription activity. Nat. Struct. Mol. Biol. *24*, 578–587. https://doi.org/10.1038/nsmb.3414.
20. Vassilev, L.T., Vu, B.T., Graves, B., Carvajal, D., Podlaski, F., Filipovic, Z., Kong, N., Kammlott, U., Lukacs, C., Klein, C., et al. (2004). In vivo activation of the p53 pathway by small-molecule antagonists of MDM2. Science *303*, 844–848. https://doi.org/10.1126/science.1092472.
21. Bertrand, E., Chartrand, P., Schaefer, M., Shenoy, S.M., Singer, R.H., and Long, R.M. (1998). Localization of ASH1 mRNA particles in living yeast. Mol. Cell *2*, 437–445. https://doi.org/10.1016/s1097-2765(00)80143-4.
22. Harton, M.D., Koh, W.S., Bunker, A.D., Singh, A., and Batchelor, E. (2019). p53 pulse modulation differentially regulates target gene promoters to regulate cell fate decisions. Mol. Syst. Biol. *15*, e8685. https://doi.org/10.15252/msb.20188685.
23. Chen, S.H., Forrester, W., and Lahav, G. (2016). Schedule-dependent interaction between anticancer treatments. Science *351*, 1204–1208. https://doi.org/10.1126/science.aac5610.
24. Brugarolas, J., Chandrasekaran, C., Gordon, J.I., Beach, D., Jacks, T., and Hannon, G.J. (1995). Radiation-induced cell cycle arrest compromised by p21 deficiency. Nature *377*, 552–557. https://doi.org/10.1038/377552a0.
25. Heltberg, M.S., Lucchetti, A., Hsieh, F.S., Minh Nguyen, D.P., Chen, S.H., and Jensen, M.H. (2022). Enhanced DNA repair through droplet formation and p53 oscillations. Cell *185*, 4394–4408.e10. https://doi.org/10.1016/j.cell.2022.10.004.
26. Swain, P.S., Elowitz, M.B., and Siggia, E.D. (2002). Intrinsic and extrinsic contributions to stochasticity in gene expression. Proc. Natl. Acad. Sci. USA *99*, 12795–12800. https://doi.org/10.1073/pnas.162041399.
27. Hafner, A., Reyes, J., Stewart-Ornstein, J., Tsabar, M., Jambhekar, A., and Lahav, G. (2020). Quantifying the Central Dogma in the p53 Pathway in Live Single Cells. Cell Syst. *10*, 495–505.e4. https://doi.org/10.1016/j.cels.2020.05.001.
28. Jiménez, A., Lu, D., Kalocsay, M., Berberich, M.J., Balbi, P., Jambhekar, A., and Lahav, G. (2022). Time-series transcriptomics and proteomics reveal alternative modes to decode p53 oscillations. Mol. Syst. Biol. *18*, e10588. https://doi.org/10.15252/msb.202110588.
29. Porter, J.R., Fisher, B.E., and Batchelor, E. (2016). p53 Pulses Diversify Target Gene Expression Dynamics in an mRNA Half-Life-Dependent Manner and Delineate Co-regulated Target Gene Subnetworks. Cell Syst. *2*, 272–282. https://doi.org/10.1016/j.cels.2016.03.006.
30. Batchelor, E., Mock, C.S., Bhan, I., Loewer, A., and Lahav, G. (2008). Recurrent initiation: a mechanism for triggering p53 pulses in response to DNA damage. Mol. Cell *30*, 277–289. https://doi.org/10.1016/j.molcel.2008.03.016.
31. Heltberg, M.L., Chen, S.H., Jiménez, A., Jambhekar, A., Jensen, M.H., and Lahav, G. (2019). Inferring Leading Interactions in the p53/Mdm2/Mdmx Circuit through Live-Cell Imaging and Modeling. Cell Syst. *9*, 548–558.e5. https://doi.org/10.1016/j.cels.2019.10.010.
32. Stewart-Ornstein, J., Iwamoto, Y., Miller, M.A., Prytyskach, M.A., Ferretti, S., Holzer, P., Kallen, J., Furet, P., Jambhekar, A., Forrester, W.C., et al. (2021). p53 dynamics vary between tissues and are linked with radiation sensitivity. Nat. Commun. *12*, 898. https://doi.org/10.1038/s41467-021-21145-z.
33. Raser, J.M., and O’Shea, E.K. (2005). Noise in gene expression: origins, consequences, and control. Science *309*, 2010–2013. https://doi.org/10.1126/science.1105891.
34. Elowitz, M.B., Levine, A.J., Siggia, E.D., and Swain, P.S. (2002). Stochastic gene expression in a single cell. Science *297*, 1183–1186. https://doi.org/10.1126/science.1070919.

35. Rodriguez, J., Ren, G., Day, C.R., Zhao, K., Chow, C.C., and Larson, D.R. (2019). Intrinsic Dynamics of a Human Gene Reveal the Basis of Expression Heterogeneity. Cell *176*, 213–226.e18. https://doi.org/10.1016/j.cell.2018.11.026.
36. Cheng, Q., Chen, L., Li, Z., Lane, W.S., and Chen, J. (2009). ATM activates p53 by regulating MDM2 oligomerization and E3 processivity. EMBO J. *28*, 3857–3867. https://doi.org/10.1038/emboj.2009.294.
37. Alt, J.R., Greiner, T.C., Cleveland, J.L., and Eischen, C.M. (2003). Mdm2 haplo-insufficiency profoundly inhibits Myc-induced lymphomagenesis. EMBO J. *22*, 1442–1450. https://doi.org/10.1093/emboj/cdg133.
38. Terzian, T., Wang, Y., Van Pelt, C.S., Box, N.F., Travis, E.L., and Lozano, G. (2007). Haploinsufficiency of Mdm2 and Mdm4 in tumorigenesis and development. Mol. Cell. Biol. *27*, 5479–5485. https://doi.org/10.1128/MCB.00555-06.
39. Hermeking, H., Lengauer, C., Polyak, K., He, T.C., Zhang, L., Thiagalingam, S., Kinzler, K.W., and Vogelstein, B. (1997). 14–3-3sigma is a p53-regulated inhibitor of G2/M progression. Mol. Cell *1*, 3–11. https://doi.org/10.1016/s1097-2765(00)80002-7.
40. Wang, X.W., Zhan, Q., Coursen, J.D., Khan, M.A., Kontny, H.U., Yu, L., Hollander, M.C., O'Connor, P.M., Fornace, A.J., Jr., and Harris, C.C. (1999). GADD45 induction of a G2/M cell cycle checkpoint. Proc. Natl. Acad. Sci. USA *96*, 3706–3711. https://doi.org/10.1073/pnas.96.7.3706.
41. Klein, A.M., Biderman, L., Tong, D., Alaghebandan, B., Plumber, S.A., Mueller, H.S., van Vlimmeren, A., Katz, C., and Prives, C. (2021). MDM2, MDMX, and p73 regulate cell-cycle progression in the absence of wild-type p53. Proc. Natl. Acad. Sci. USA *118*, e2102420118. https://doi.org/10.1073/pnas.2102420118.
42. Lahav, G., Rosenfeld, N., Sigal, A., Geva-Zatorsky, N., Levine, A.J., Elowitz, M.B., and Alon, U. (2004). Dynamics of the p53-Mdm2 feedback loop in individual cells. Nat. Genet. *36*, 147–150. https://doi.org/10.1038/ng1293.
43. Nelson, D.E., Ihekwaba, A.E., Elliott, M., Johnson, J.R., Gibney, C.A., Foreman, B.E., Nelson, G., See, V., Horton, C.A., Spiller, D.G., et al. (2004). Oscillations in NF-kappaB signaling control the dynamics of gene expression. Science *306*, 704–708. https://doi.org/10.1126/science.1099962.
44. Seidman, J.G., and Seidman, C. (2002). Transcription factor haploinsufficiency: when half a loaf is not enough. J. Clin. Invest. *109*, 451–455. https://doi.org/10.1172/JCI15043.
45. Cao, Y., Lopatkin, A., and You, L. (2016). Elements of biological oscillations in time and space. Nat. Struct. Mol. Biol. *23*, 1030–1034. https://doi.org/10.1038/nsmb.3320.
46. Tsai, T.Y., Choi, Y.S., Ma, W., Pomerening, J.R., Tang, C., and Ferrell, J.E., Jr. (2008). Robust, tunable biological oscillations from interlinked positive and negative feedback loops. Science *321*, 126–129. https://doi.org/10.1126/science.1156951.
47. Paszek, P., Ryan, S., Ashall, L., Sillitoe, K., Harper, C.V., Spiller, D.G., Rand, D.A., and White, M.R. (2010). Population robustness arising from cellular heterogeneity. Proc. Natl. Acad. Sci. USA *107*, 11644–11649. https://doi.org/10.1073/pnas.0913798107.
48. Kellogg, R.A., and Tay, S. (2015). Noise facilitates transcriptional control under dynamic inputs. Cell *160*, 381–392. https://doi.org/10.1016/j.cell.2015.01.013.
49. Geva-Zatorsky, N., Dekel, E., Batchelor, E., Lahav, G., and Alon, U. (2010). Fourier analysis and systems identification of the p53 feedback loop. Proc. Natl. Acad. Sci. U SA *107*, 13550–13555. https://doi.org/10.1073/pnas.1001107107.
50. Kim, J.K., and Forger, D.B. (2012). A mechanism for robust circadian timekeeping via stoichiometric balance. Mol. Syst. Biol. *8*, 630. https://doi.org/10.1038/msb.2012.62.
51. Stewart-Ornstein, J., and Lahav, G. (2017). p53 dynamics in response to DNA damage vary across cell lines and are shaped by efficiency of DNA repair and activity of the kinase ATM. Sci. Signal. *10*, eaah6671. https://doi.org/10.1126/scisignal.aah6671.
52. Friedrich, D., Friedel, L., Finzel, A., Herrmann, A., Preibisch, S., and Loewer, A. (2019). Stochastic transcription in the p53-mediated response to DNA damage is modulated by burst frequency. Mol. Syst. Biol. *15*, e9068. https://doi.org/10.15252/msb.20199068.
53. Sánchez, Y., Segura, V., Marín-Béjar, O., Athie, A., Marchese, F.P., González, J., Bujanda, L., Guo, S., Matheu, A., and Huarte, M. (2014). Genome-wide analysis of the human p53 transcriptional network unveils a lncRNA tumour suppressor signature. Nat. Commun. *5*, 5812. https://doi.org/10.1038/ncomms6812.
54. Schindelin, J., Arganda-Carreras, I., Frise, E., Kaynig, V., Longair, M., Pietzsch, T., Preibisch, S., Rueden, C., Saalfeld, S., Schmid, B., et al. (2012). Fiji: an open-source platform for biological-image analysis. Nat. Methods *9*, 676–682. https://doi.org/10.1038/nmeth.2019.
55. Schmidt, U., Weigert, M., Broaddus, C., and Myers, G. (2018). Cell Detection with Star-Convex Polygons. held in Cham, A.F. Frangi, J.A. Schnabel, C. Davatzikos, C. Alberola-López, and G. Fichtinger, eds. (Springer International Publishing), pp. 265–273.
56. Berg, S., Kutra, D., Kroeger, T., Straehle, C.N., Kausler, B.X., Haubold, C., Schiegg, M., Ales, J., Beier, T., Rudy, M., et al. (2019). ilastik: interactive machine learning for (bio)image analysis. Nat. Methods *16*, 1226–1232. https://doi.org/10.1038/s41592-019-0582-9.
57. Grinsted, A., Moore, J.C., and Jevrejeva, S. (2004). Application of the cross wavelet transform and wavelet coherence to geophysical time series. Nonlin. Processes Geophys. *11*, 561–566. https://doi.org/10.5194/npg-11-561-2004.
58. Legland, D., Arganda-Carreras, I., and Andrey, P. (2016). MorphoLibJ: integrated library and plugins for mathematical morphology with ImageJ. Bioinformatics *32*, 3532–3534. https://doi.org/10.1093/bioinformatics/btw413.
59. Michalk, M., Meinrath, J., Künstlinger, H., Koitzsch, U., Drebber, U., Merkelbach-Bruse, S., Bollschweiler, E., Kloth, M., Hartmann, W., Hölscher, A., et al. (2016). MDM2 gene amplification in esophageal carcinoma. Oncol. Rep. *35*, 2223–2227. https://doi.org/10.3892/or.2016.4578.
60. Raj, A., Peskin, C.S., Tranchina, D., Vargas, D.Y., and Tyagi, S. (2006). Stochastic mRNA synthesis in mammalian cells. PLoS Biol. *4*, e309. https://doi.org/10.1371/journal.pbio.0040309.
61. Golding, I., Paulsson, J., Zawilski, S.M., and Cox, E.C. (2005). Real-time kinetics of gene activity in individual bacteria. Cell *123*, 1025–1036. https://doi.org/10.1016/j.cell.2005.09.031.
62. Batchelor, E., Loewer, A., Mock, C., and Lahav, G. (2011). Stimulus-dependent dynamics of p53 in single cells. Mol. Syst. Biol. *7*, 488. https://doi.org/10.1038/msb.2011.20.
63. Zhang, T., Brazhnik, P., and Tyson, J.J. (2007). Exploring mechanisms of the DNA-damage response: p53 pulses and their possible relevance to apoptosis. Cell Cycle *6*, 85–94. https://doi.org/10.4161/cc.6.1.3705.
64. Mengel, B., Hunziker, A., Pedersen, L., Trusina, A., Jensen, M.H., and Krishna, S. (2010). Modeling oscillatory control in NF-kappaB, p53 and Wnt signaling. Curr. Opin. Genet. Dev. *20*, 656–664. https://doi.org/10.1016/j.gde.2010.08.008.
65. Sun, T., and Cui, J. (2014). A plausible model for bimodal p53 switch in DNA damage response. FEBS Lett. *588*, 815–821. https://doi.org/10.1016/j.febslet.2014.01.044.
66. Gillespie, D.T. (1977). Exact stochastic simulation of coupled chemical reactions. J. Phys. Chem. *81*, 2340–2361. https://doi.org/10.1021/j100540a008.
67. Gonze, D., Halloy, J., and Goldbeter, A. (2002). Robustness of circadian rhythms with respect to molecular noise. Proc. Natl. Acad. Sci. USA *99*, 673–678. https://doi.org/10.1073/pnas.022628299.
68. Cheng, M.-Y., and Hall, P. (1998). Calibrating the Excess Mass and Dip Tests of Modality. J. R. Stat. Soc. B *60*, 579–589.

STAR★METHODS

KEY RESOURCES TABLE

REAGENT or RESOURCE	SOURCE	IDENTIFIER
Antibodies		
Mouse monoclonal anti-Mdm2 (SMP14)	Santa Cruz Biotechnology	Cat#sc-965; RRID: AB_627920
Mouse monoclonal anti-Mdm2 (HDM2-323)	Santa Cruz Biotechnology	Cat#sc-56154; RRID: AB_784462
Rabbit monoclonal anti-Mdm2 antibody (D1V2Z)	Cell Signaling Technology	Cat#86934; RRID: AB_2784534
Rabbit polyclonal anti-p53 antibody (FL-393)	Santa Cruz Biotechnology	Cat#sc-6243; RRID: AB_653753
Mouse monoclonal anti-p53 antibody (DO-1)	Santa Cruz Biotechnology	Cat#sc-126; RRID: AB_628082
Rabbit monoclonal anti-p21 antibody (12D1)	Cell Signaling Technology	Cat#2947; RRID: AB_823586
GFP tag antibody	Proteintech	Cat#50430-2-AP; RRID: AB_11042881
Mouse monoclonal anti-actin antibody	Millipore	Cat#MAB1501; RRID: AB_2223041
Normal mouse IgG	Sigma-Aldrich	Cat#12-371; RRID: AB_145840
Goat anti-Mouse IgG (H+L) Highly Cross-Adsorbed Secondary Antibody, Alexa Fluor™ Plus 647	Thermo Fisher Scientific	Cat#A32728; RRID: AB_2633277
Goat anti-Rabbit IgG (H+L) Highly Cross-Adsorbed Secondary Antibody, Alexa Fluor™ Plus 647	Thermo Fisher Scientific	Cat#A32733; RRID: AB_2633282
Goat anti-Rabbit IgG (H+L) Highly Cross-Adsorbed Secondary Antibody, Alexa Fluor™ 594	Thermo Fisher Scientific	Cat#A11037; RRID: AB_2534095 AB_2354095
IRDye 800CW Goat anti-Rabbit IgG Secondary Antibody	LI-COR Biosciences	Cat#926-32211; RRID: AB_621843
IRDye 680RD Goat anti-Mouse IgG Secondary Antibody	LI-COR Biosciences	Cat#926-68070; RRID: AB_10956588
Bacterial and virus strains		
pEF1α-Mdm2-GS1-SYFP2 (lentiviral)	This paper	This paper
pEF1α-Mdm2-GS4-SYFP2 (lentiviral)	This paper	This paper
pEF1α-Mdm2-GS8-SYFP2 (lentiviral)	This paper	This paper
pEF1α-Mdm2-GA-SYFP2 (lentiviral)	This paper	This paper
pEF1α-Mdm2-flexible-SYFP2 (lentiviral)	This paper	This paper
pEF1α-Mdm2-EA4-SYFP2 (lentiviral)	This paper	This paper
pEF1α-Mdm2-PA-SYFP2 (lentiviral)	This paper	This paper
UbC NLS-HA-MCP-mCherry (lentiviral)	This paper	This paper
CSII-EF-mCherry-hGeminin(1-110) (lentiviral)	Reyes et al.[8]	N/A
Chemicals, peptides, and recombinant proteins		
Neocarzinostatin (NCS)	Sigma-Aldrich	N9162
Nutlin-3a	Sigma-Aldrich	SML0580
Cycloheximide	Sigma-Aldrich	C7698
DAPI [4,6-Diamidino-2-phenylindole, dihydrochloride]	AAT Bioquest	17510
Paraformaldehyde 16% (w/v) in aqueous solution methanol-free	Thermo Fisher Scientific	43368
DPBS (10X), no calcium, no magnesium	Gibco	14200075
RPMI 1640 Media	Gibco	11875093
DMEM, high glucose	Gibco	11965084
Antibiotic-Antimycotic (100X)	Gibco	15240062
Characterized FBS, Canadian Origin	HyClone	SH30396.03
Albumin, Bovine Serum, Fraction V, low Heavy Metals (BSA)	Sigma-Aldrich	12659
Triton X-100 Reagent Grade	BioShop	TRX506
VECTASHIELD Antifade Mounting Medium	Vector Laboratories	H-1000
UltraPure SSC, 20X	Thermo Fisher Scientific	15557044

(*Continued on next page*)

Continued

REAGENT or RESOURCE	SOURCE	IDENTIFIER
Formamide	Merck	1.09684.1000
Diethyl pryocarbonate (DEPC)	Sigma-Aldrich	D5758
SiR-DNA kit	Spirochrome	SC007
SiR700-DNA Kit	Spirochrome	SC015
NEBuilder HiFi DNA Assembly	NEB	E2621S
FuGENE HD Transfection Reagent	Promega	E2312
DharmaFECT 1 Transfection Reagent	Dharmacon	T-2001
LR Clonase II Plus enzyme	Thermo Fisher Scientific	12538120
Gateway BP Clonase II Enzyme mix	Thermo Fisher Scientific	11789
Hygromycin B Gold (solution)	InvivoGen	ant-hg-1
Blasticidin (solution)	InvivoGen	ant-bl-1
Alt-R CRISPR-Cas9 tracrRNA	Integrated DNA Technologies	1072532
Alt-R S.p. HiFi Cas9 Nuclease V3	Integrated DNA Technologies	1081060
EZ-PCR Mycoplasma Detection Kit	Biological Industries	20-700-20
PureLink RNase A	Thermo Fisher Scientific	12091021
Proteinase K	Thermo Fisher Scientific	25530049
Dynabeads Protein G for Immunoprecipitation	Thermo Fisher Scientific	10004D
iQ SYBR Green Supermix	Bio-Rad	1708882
Duolink PLA Probe Anti-Mouse PLUS	Sigma-Aldrich	DUO92001
Duolink PLA Probe Anti-Rabbit MINUS	Sigma-Aldrich	DUO92005
Duolink In Situ Mounting Medium with DAPI	Sigma-Aldrich	DUO82040
Critical commercial assays		
SE Cell Line 4D-Nucleofector X Kit L	Lonza Bioscience	V4XC-1024
SF Cell Line 4D-Nucleofector X Kit L	Lonza Bioscience	V4XC-2012
P3 Primary Cell 4D-Nucleofector X Kit L	Lonza Bioscience	V4XP-3024
QIAquick PCR purification kit	Qiagen	28106
QIAamp DNA Mini Kit	Qiagen	51306
DuoLink PLA	Sigma-Aldrich	DUO92008
Experimental models: Cell lines		
MCF7 + p53shRNA + pEF1α-p53-mCerulean	Gaglia et al.[16]	N/A
A549 + UbCp-p53-mVenus	Stewart-Ornstein and Lahav[51]	N/A
RPE-1 + UbCp-p53-mNeonGreen	Reyes et al.[8]	N/A
MCF7 p53-Mdm2 reporter: MCF7 + p53shRNA + pEF1α-p53-mCerulean + Mdm2-PA-SYFP2-P2A-Hygro (endogenous tag)	This paper	This paper
MCF7 p53-Mdm2 reporter/Geminin-mCherry: MCF7 + p53shRNA + pEF1α-p53-mCerulean + CSII-EF-mCherry-hGeminin(1-110) + Mdm2-PA-SYFP2-P2A-Hygro (endogenous tag)	This paper	This paper
MCF7 Mdm2-protein-RNA reporter: MCF7 + p53shRNA + pEF1α-p53-mCerulean + UbC NLS-HA-MCP-mCherry + Mdm2-PA-SYFP2-24xMS2 (endogenous tag)	This paper	This paper
MCF7 *MDM2* dual-allele reporter: MCF7 + p53shRNA + pEF1α-p53-mCerulean + UbC NLS-HA-MCP-mCherry + Mdm2-PA-SYFP2-P2A-Hygro + Mdm2-P2A-Blast-24xMS2 (endogenous tag)	This paper	This paper
A549 p53-Mdm2 reporter: A549 + UbCp-p53-mVenus + Mdm2-PA-mCerulean-P2A-Blast (endogenous tag)	This paper	This paper

(*Continued on next page*)

Continued

REAGENT or RESOURCE	SOURCE	IDENTIFIER
RPE-1 p53-Mdm2 reporter: RPE-1 + UbCp-p53-mNeonGreen + Mdm2-PA-mCerulean-P2A-Blast (endogenous tag)	This paper	This paper
HEK293T cells	ATCC	Cat#CRL-3216; RRID: CVCL_0063
Oligonucleotides		
MDM2 gRNA: TCTTATAGACAGGTCAACTA	Stewart-Ornstein and Lahav[51]	N/A
MDM2 WT Forward (for genotyping): 5’-GTAG CATTATTTATAGCAGCCAAGA-3’	Integrated DNA Technologies	This paper
MDM2 WT Reverse (for genotyping): 5’-CTAT GTGAATTGAGGCATTTTCTCAC-3’	Integrated DNA Technologies	This paper
FP Reverse (for genotyping): 5’-TTGAAGAA GTCGTGCTGCTTC-3’	Integrated DNA Technologies	This paper
Blast Reverse (for genotyping): 5’-ATGCAG ATCGAGAAGCACC-3’	Integrated DNA Technologies	This paper
siRNA for Control knockdown (ON-TARGETplus Non-targeting siRNA): UGGUUUACAUGUCGACUAA	Dharmacon	D-001810-01-20
siRNA for *MDM2* single-allele knockdown: GGAUAUGUCCUGCGGGUAAUU	Dharmacon, Custom siRNA	This paper
siRNA for *MDM2* double-allele knockdown: GAACAAGAGACCCUGGUUA	Dharmacon	J-003279-12-0005
siRNA for *TP53* knockdown (SMARTpool): GAAAUUUGCGUGUGGAGUA GUGCAGCUGUGGGUUGAUU GCAGUCAGAUCCUAGCGUC GGAGAAUAUUUCACCCUUC	Dharmacon	L-003329-00-0005
smFISH probe against *MDM2* exon regions	Friedrich et al.[52]	N/A
BAC-derived DNA FISH probes against *MDM2*	Empire Genomics	RP11-1137N1
Untagged *MDM2* Forward (qPCR) 5-‘AATAAGCCCTGCCCAGTATG-3’	Integrated DNA Technologies	This paper
Untagged *MDM2* Reverse (qPCR) 5’-CAGGTTGTCTAAATTCCTAGGGT-3’	Integrated DNA Technologies	This paper
RPP30 Forward (qPCR) 5’-AGTGGTAGTGCATAGACTTTA-3’	Integrated DNA Technologies	N/A
RPP30 Reverse (qPCR) 5’-GTAGGAGGACATTTGAGGAG-3’	Integrated DNA Technologies	N/A
MDM2 forward (for ChIP assay): 5’-GTTCAGTGGGCAGGTTGACT-3’	Sánchezet al. [53]	N/A
MDM2 reverse (for ChIP assay): 5’-CAATCGCCACTGAACACAGC-3’	Integrated DNA Technologies	This paper
Recombinant DNA		
pCR4-24XMS2SL-stable	Addgene	31865
UbC NLS-HA-MCP-YFP	Addgene	31230
UbC NLS-HA-MCP-mCherry	This paper	This paper
MDM2 homology-PA-SYFP2-P2A-Hygro-*MDM2* homology	This paper	This paper
MDM2 homology-PA-mCerulean-P2A-Blast-*MDM2* homology	This paper	This paper
MDM2 homology-PA-SYFP2-24xMS2-*MDM2* homology	This paper	This paper
MDM2 homology-P2A-Blast-24xMS2-*MDM2* homology	This paper	This paper

(*Continued on next page*)

Continued

REAGENT or RESOURCE	SOURCE	IDENTIFIER
Software and algorithms		
MATLAB (2020b)	The Mathworks Inc.	https://matlab.mathworks.com/
Fiji	Schindelin et al.[54]	https://fiji.sc/
MetaXpress High Content Image Acquisition & Analysis Software version 6.6.3.55	Molecular Devices	N/A
Single cell tracking algorithm	Reyes et al.[8]	https://github.com/balvahal/p53CinemaManual
StarDist	Schmidt et al.[55]	https://github.com/stardist/stardist
Ilastik	Berg et al.[56]	https://www.ilastik.org/index.html
Wavelet coherence toolbox	Grinsted et al.[57]	http://grinsted.github.io/wavelet-coherence/
MorphoLibJ	Legland et al.[58]	https://github.com/ijpb/MorphoLibJ
Mdm2 pulse skipping detection algorithm	This paper	https://doi.org/10.5281/zenodo.13743894
Sensitivity analysis algorithm	This paper	https://doi.org/10.5281/zenodo.13743894
MS2 quantification algorithm	This paper	https://doi.org/10.5281/zenodo.13743894
smFISH quantification algorithm	This paper	https://doi.org/10.5281/zenodo.13743894

EXPERIMENTAL MODEL AND SUBJECT DETAILS

Cell culture

HEK293T cells were purchased from American Type Culture Collection (ATCC) and cultured according to ATCC's instructions. MCF7 (MCF7 + p53shRNA + pEF1α -p53-mCerulean),[16] A549 (A549 + UbCp-p53-mVenus),[51] and RPE-1 (RPE-1 + UbCp-p53-mNeonGreen)[8] cells were maintained in RPMI 1640 media. All cell lines were grown in culture media supplemented with 5% FBS and antibiotics (100 units/mL of penicillin, 100 μg/mL of streptomycin, and 0.25 μg/mL of Gibco Amphotericin B) in a humidified incubator at 37°C with 5% CO_2. All cell lines used in the study were confirmed to be mycoplasma-free.

Gene targeting and reporter cell development

Gene targeting was conducted using the Alt-R CRISPR-Cas9 crRNA:tracrRNA system (Integrated DNA Technologies). To endogenously tag *MDM2* at its C-terminus with a fluorescent protein, we performed nucleofection on parental cells (MCF7 + p53shRNA + pEF1α-p53-mCerulean, A549 + UbCp-p53-mVenus, and RPE-1 + UbCp-p53-mNeonGreen) with ribonucleoprotein (RNP, composed of a two-part gRNA and recombinant Cas9 enzyme targeting the *MDM2* C-terminus region) and a linearized homology donor (*MDM2* homology-PA-SYFP2-P2A-Hygro-*MDM2* homology or *MDM2* homology-PA-mCerulean-P2A-Blast-*MDM2* homology). Nucleofection was performed in a 4D-Nucleofector system (Lonza Bioscience) according to the manufacturer's instructions. Individual clonal cells after antibiotic selection were verified by genotyping PCR and sequencing (Figures S1E and S1K). In order to monitor cell cycle re-entry in the MCF7 p53-Mdm2 reporter, the cell line was further infected with CSII-EF-mCherry-hGeminin(1-110) lentiviral vector, which was modified from CSII-EF-mVenus-hGeminin(1-110).[8]

To establish the Mdm2-protein-RNA cell line, we first infected the parental cells (MCF7 + p53shRNA + pEF1α-p53-mCerulean) with the lentiviral vector UbC NLS-HA-MCP-mCherry. Fluorescence-activated cell sorting (FACS) was performed to enrich for the cell population expressing mCherry. Next, the cells were nucleofected with RNP targeting specific loci in the *MDM2* C-terminus and a linearized homology donor (*MDM2* homology-PA-SYFP2-24xMS2-*MDM2* homology). Cells were treated with a low dose of Nutlin-3a (4 μM, 4 hours) to transiently induce Mdm2-SYFP2 levels, followed by FACS to enrich for the population of cells expressing SYFP2. Clonal cells were further screened for the presence of nuclear MCP-mCherry fluorescent foci after DSBs.

To generate the *MDM2* dual-allele reporter cell line, we first infected the MCF7 p53-Mdm2 reporter cells with the lentiviral vector UbC NLS-HA-MCP-mCherry and then performed FACS to enrich for the population of cells displaying mCherry fluorescence. Next, the cells were nucleofected with RNP targeting the untagged *MDM2* alleles with a linearized homology donor (*MDM2* homology-P2A-Blast-24xMS2-*MDM2* homology). The resulting tagged coding sequence includes a blasticidin resistance gene, enabling antibiotic selection. After blasticidin selection, clonal cells were further screened for the presence of nuclear MCP-mCherry fluorescent foci after DSBs.

METHOD DETAILS

siRNA knockdown

Control siRNA (D-001810-01-20) and p53 SMARTpool siRNA (L-003329-00-0005) were purchased from Dharmacon. For *MDM2* single-allelic knockdown, the siRNA was designed against the hygromycin-resistant gene. This siRNA allowed specific knockdown of *MDM2*-SYFP2-P2A-Hygro allele expression (Figure 1A; also see Figure S1D), but not the untagged allele in p53-Mdm2 reporter cells. DharmaFECT 1 (Dharmacon) was used for siRNA transfection according to the manufacturer's instructions. Media was replaced 8-12 hours post siRNA delivery to reduce toxicity from the transfection reagents.

Plasmids and cloning

The Mdm2 overexpression constructs (pEF1α-Mdm2-linker-SYFP2) were generated using a Gateway cloning system (Invitrogen). Briefly, three entry clones containing the EF1α-Mdm2 sequence, a linker (see Figure S1A for the linker information), and the SYFP2 sequence were combined with the lentiviral destination vector to create the desired clones. The *MDM2* homology regions—469 basepairs (bp) upstream (excluding the STOP codon) and 386 bp downstream of the insertion site—were amplified by polymerase chain reaction (PCR) from genomic DNA and verified by sequencing. Insertion sequences (e.g., PA-SYFP2-P2A-Hygro) were then inserted in-frame with the *MDM2* upstream homology region using an NEBuilder HiFi DNA Assembly kit (NEB). The MS2 stem loop sequence was obtained from Addgene plasmid (#31865). UbC NLS-HA-MCP-mCherry was generated by replacing the YFP sequence with mCherry in UbC NLS-HA-MCP-YFP from Addgene (#31230).

Imaging-based assessment of Mdm2-linker-SYFP2 localization and stability

To mitigate the effect of the C-terminal tag (linker + fluorescent protein) on the half-life and localization of Mdm2, we developed an overexpression system for imaging-based measurements. Parental cells (MCF7 + p53shRNA + pEF1α-p53-mCerulean) were infected with pEF1α-Mdm2-linker-SYFP2 lentivirus and assessed for Mdm2-linker-SYFP2 expression after at least two passages. To measure Mdm2 protein stability, cells were treated with 2.5 μg/ml cycloheximide (Sigma) and imaged every 10 minutes for 15 hours using a 20x objective under a Nikon eclipse Ti microscope. The nuclei were labeled with a SiR-DNA probe (Spirochrome, diluted 1:40,000 in RPMI without riboflavin and phenol red). Half-life of the nuclear Mdm2-linker-SYFP2 signal was determined by identifying the time at which the SYFP2 signal intensity reached 50% of the original signal before cycloheximide treatment.

DNA Fluorescence In Situ Hybridization (DNA FISH)

MDM2 (RP11-1137N1) BAC DNA FISH probes were purchased from Empire Genomics labeled with 5-ROX fluorescent dye. Cells were plated at a density of 10,000 cells per well in an 8-well glass chamber slide (Millipore, PEZGS0816) one day before fixation. The staining was performed based on manufacturer's protocol with a minor modification. Briefly, samples were permeabilized with 70% ethanol for at least 1 hour at 4°C, followed by a 5-minute wash in wash buffer A (2x SSC and 10% formamide in nuclease-free water). Samples were then dehydrated through 70%, 85%, and 100% ethanol prior to FISH probe hybridization. Denaturation was done at 73°C for 2 minutes. Hybridization was performed overnight at 37°C in a dark humidified chamber. Samples were washed once with wash buffer B (0.4x SSC and 0.3% Igepal in nuclease-free water) at 60°C for 2 minutes, followed by a wash in wash buffer C (2x SSC and 0.1% Igepal in nuclease-free water) at room temperature for 2 minutes each. After drying the slide, samples were mounted with DAPI with antifade. Images were taken with 0.25 μm step-width z-stacks spanning at least 6 μm with a 40× objective on a Zeiss LSM 710 confocal microscope with 561 nm laser excitation and detection gating from 575 to 620 nm. For data visualization, cells in focus were maximum-projected, followed by deconvolution and gamma correction to sharpen the DNA FISH foci.

Quantitative PCR for determining gene copy number

To assess the copy number of untagged and tagged *MDM2* alleles in the constructed p53-Mdm2 reporters, we followed previously described qPCR methods with some modifications.[59] Primers targeting the C-terminus of *MDM2* genomic loci were designed to amplify untagged regions. Ribonuclease P protein subunit p30 (*RPP30*) was used as an internal reference gene, as it possesses the same copy number across different samples. The assays were performed in triplicate with iQ SYBR Green Supermix (BioRad) using 0.39 to 100 ng of genomic DNA in a 10 μL reaction. qPCR was carried out using a BioRad CFX Opus 96 Real-Time PCR System with a PCR program (5 minutes at 95°C hot start, 45 cycles of 10 seconds denaturing at 95°C, 30 seconds annealing-elongation at 61 °C). Amplification efficiency was determined for all primer sets and fell within a range of 90-110%, indicating a lack of bias in the copy number quantification model based on starting template abundance. Melting curve analysis was conducted to confirm a single peak for the amplicon, indicating high primer specificity. Relative quantity of untagged *MDM2* alleles in test samples was determined by the comparative $\Delta\Delta C_T$ method using the following equations:

$$\Delta \mathrm{Ct} = (\mathrm{Ct})_{\mathrm{Untagged}\ MDM2} - (\mathrm{Ct})_{RPP30}$$

$$\Delta\Delta \mathrm{Ct} = (\Delta \mathrm{Ct})_{\mathrm{Test\ sample}} - (\Delta \mathrm{Ct})_{\mathrm{Reference\ sample}}$$

$$\text{The gene copy number} = 2^{-\Delta\Delta \mathrm{Ct}} \times 1$$

The reference sample (RPE-1 p53-Mdm2 reporter) is known to have one copy of an untagged and one copy of a tagged *MDM2* allele based on genotyping (Figure S1K) and DNA FISH (Figure S3C) results, respectively.

Immunoblotting

Cells were harvested with ice-cold RIPA buffer supplemented with protease inhibitor cocktail (Sigma). Samples (40 μg) were subjected to standard SDS-PAGE immunoblotting. Antibody dilution rates were: Mdm2 (SMP14, 1:100); p53 (FL-393, 1:1,000); actin (1:100,000); GFP (1:4,000); and IRDye 800CW Goat anti-Rabbit IgG and IRDye 680RD Goat anti-Mouse IgG secondary antibodies (LI-COR Biosciences, 1:40,000). Images were acquired using an Amersham Typhoon 5 system. Protein bands were quantified using Fiji.[54]

Immunofluorescence

Cells were fixed in 4% paraformaldehyde, permeabilized with 1% Triton X-100, blocked with 2% BSA, and stained with the primary antibody overnight at 4°C. Goat anti-mouse or goat anti-rabbit secondary antibody conjugated with Alexa Fluor 647 (Thermo Fisher Scientific, 1:1,000) or Alexa Fluor 594 (Thermo Fisher Scientific, 1:1:1,000) was used to visualize the target protein. DAPI was used for nucleus staining to support nuclear segmentation. Images were taken using an ImageXpress Micro XL High-Content Screening System with a 20x objective and analyzed using MetaXpress software. Filter sets: Cy5 (ex:628/40; em:692/40), Texas Red (ex:562/40; em:624/40) and DAPI (ex:377/50; em:447/60). Antibody dilution rates were: Mdm2 (HDM2-323, 1:1,000); p21 (12D1, 1:1,000).

Live-cell microscopy

Cells were plated at 2,000 cells/well in a μ-Plate 96 Well Black plate (ibidi Cat#89626) or 6,000-8,000 cells/well in a 24-well glass-bottom plate (MatTek, P24G-1.0-13-F) one day before imaging. Cells were imaged in transparent RPMI (RPMI without riboflavin and phenol red, customized by USBiological) containing SiR700-DNA probe (Spirochrome, 1:40,000). Images were acquired every 30 minutes on a Nikon eclipse Ti microscope using a 20x objective in a humidified chamber at 37°C, 5% CO_2.

Neocarzinostatin (NCS; Sigma, 200–400 ng/ml) or 10Gy γ-irradiation was introduced to induce p53/Mdm2 oscillations. To achieve transient Mdm2 induction and to block p53-Mdm2 interaction, 3 μM and 0.75 μM Nutlin-3a (Sigma) were added 5 and 10 hours after NCS treatment, respectively. To image *MDM2* transcriptional foci, images were taken every 5 minutes using a 40x objective. Five z-stacks spanning 3.2 μm were collected. Filter sets: SiR700 (ex:640/30; em:700/75), mCherry (ex:575/25; em:647/57), SYFP2 or mNeonGreen (ex:510/25; em:544/24), mCerulean (ex:440/20; em:483/32).

Proximity ligation assay (PLA)

Formation of the p53-Mdm2 complex was examined using Duolink *In Situ* Detection Reagents Red (Sigma) following the manufacturer's instructions. Briefly, cells were seeded at a density of 5,000 cell per well in an 8-well glass chamber slide (Millipore, PEZGS0816) two days prior to treatment and fixation. The fixed samples were incubated with primary antibodies against mouse monoclonal p53 (DO-1, 1:1,000) and rabbit monoclonal Mdm2 (D1V2Z, 1:1,000). Following the manufacturer's protocol, the samples were then washed and subjected to PLA probes (Sigma, DUO92001 and DUO92005) incubation, ligation, and amplification. Finally, the slide was mounted with a coverslip using a minimal volume of Duolink *In Situ* Mounting Medium with DAPI (Sigma, DUO82040). Image acquisition was performed on a Zeiss LSM 710 confocal microscope under a 40x/oil objective, and at least six *z*-stacks spanning 6 μm were collected in the Texas Red and DAPI channels. To quantify PLA signals, we applied maximal projection to the mCherry z-stacks and quantified the total intensity of the PLA signals inside the nucleus.

Chromatin Immunoprecipitation and quantitative real-time PCR (ChIP-qPCR)

5 x 10^6 cells per condition were fixed in 1% formaldehyde for 15 minutes. The cross-linking reaction was stopped by adding glycine at a final concentration of 125 mM for 5 minutes at room temperature. Cells were then washed three times in cold PBS, harvested with 1 ml lysis buffer 1 (50 mM HEPES pH7.5, 140 mM NaCl, 1 mM EDTA pH8.0, 10% Glycerol, 0.5% Igepal CA630, 0.25% Triton X-100), and incubated for 10 minutes on a rotating wheel at 4°C. Cells were then centrifuged at 1,350 x g for 5 minutes at 4°C. The supernatant was aspirated, and the pellet was resuspended with 1 ml lysis buffer 2 (10 mM Tris-HCl pH8.0, 200 mM NaCl, 1 mM EDTA pH8.0, 0.5 mM EGTA pH8.0), followed by a 10-minute incubation on a rotating wheel at 4°C. Cells were centrifuged again at 1,350 x g for 5 minutes at 4°C, and the pelleted nuclei were resuspended in 1 ml sonication buffer (50 mM HEPES pH7.5, 140 mM NaCl, 1 mM EDTA pH8.0, 1 mM EGTA pH8.0, 1% Triton X-100, 0.1% SDS, 0.1% Sodium deoxycholate). Chromatin was sonicated using a Covaris E220 evolution sonicator (Peak Power 140, Duty Factor 5.0, Cycle/Burst 200, Duration 600 seconds). Sheared chromatin (10 μl) was saved as 2% input. The ~1 ml sonicated samples were precleared by incubating with 5 μg of normal mouse IgG (Sigma) and 25 μl of Dynabeads protein G (Invitrogen) for 2 hours on a rotating wheel at 4°C. The precleared chromatin was then incubated with 5 μg of p53 antibody (DO-1), Mdm2 antibody (SMP14), or control IgG for 3 hours. Dynabeads protein G (25 μl) was added to the samples and incubated on a rotating wheel overnight at 4°C. Beads were washed twice with sonication buffer, once with high salt sonication buffer (50 mM HEPES pH7.5, 500 mM NaCl, 1 mM EDTA pH8.0, 1 mM EGTA pH8.0, 1% Triton X-100, 0.1% SDS, 0.1% Sodium deoxycholate), once with LiCl wash buffer (10 mM Tris-HCl pH8.0, 1 mM EDTA, 250 mM LiCl, 1% Igepal CA630, 1% Sodium deoxyycholate), and twice with TE buffer (10 mM Tris-HCl pH8.0, 1 mM EDTA, pH8.0). The aforementioned buffers were supplemented with protease inhibitor cocktail (Sigma) before use. The DNA was eluted from the beads with two sequential additions of ChIP elution buffer (1% SDS, 0.1 M $NaHCO_3$), followed by incubation at 37°C for 30 minutes. Reverse crosslinking was done by adding 200 mM NaCl and incubation at 65°C overnight. Input samples were processed identically. RNA and protein in the samples were further digested by addition of RNase A (50 μg/ml, 37°C for 30 minutes), followed by Proteinase

K digestion (50 μg/ml, 65°C for 1 hour). The DNA was cleaned up with a Qiagen PCR purification kit according to the manufacturer's protocol.

Quantitative real-time PCR (qPCR) was performed in a 10 μl reaction containing 5 μl iQ SYBR Green Supermix (BioRad), 2 μl eluted DNA, 2.5 μl H_2O, and 0.5 μl of 10 mM primers (primer sequences are provided in the Key Resources Table). qPCR was carried out using a BioRad CFX Opus 96 Real-Time PCR System with a PCR program (3 minutes at 95°C hot start, 45 cycles of 10 seconds denaturing at 95°C, 30 seconds annealing-elongation at 61°C). Melting curves were conducted after amplification to verify the fluorescence detected during the run from a single amplicon. The resulting data were normalized to the input DNA and calculated as % of input using the following equation:

$$\%\ \text{input} = 2^{(Ct''\text{Input}'' - Ct''IP'')} \times 100$$

Single-molecule FISH

Cells were fixed 2.5 hours after treatment with 4% paraformaldehyde (PFA) and permeabilized with 70% ethanol. Hybridization was performed overnight at 37°C in hybridization buffer (10% dextran sulfate, 2x SSC, and 10% formamide in DEPC-treated water) containing 125 nM smFISH probes (Biosearch Technologies) against *MDM2* exonic regions, as described previously.[52] Samples were washed twice with wash buffer (2x SSC and 10% formamide in DEPC-treated water) and fixed again with 4% PFA in 2x SSC for 30 minutes at 37°C, followed by two washes in 2x SSC. After DAPI staining, samples were mounted with antifade mounting media (Vector Laboratories) and imaged with a 40x objective. Twenty-one z-stacks spanning 4 μm were collected in the Cy5 channel.

To quantify smFISH signal, we first applied maximal projection to the Cy5 z-stacks. Then, we performed pseudo flat-field correction with a blurring radius of 50 pixels using BioVoxxel, as well as background subtraction with a rolling-ball radius of 50 pixels, using Fiji. Cell nuclei were segmented according to the DAPI channel using StarDist, followed by manual curation. For each nucleus, we took the pixel with the strongest *MDM2*-MS2 signal, and then searched within a radius of 25 pixels in the Cy5 channel. The smFISH signal of said nucleus was defined as the mean Cy5 intensity of the three brightest pixels, normalized to the median nuclear intensity.

Single-cell tracking

Individual cells were tracked either semi-automatically using a previously established MATLAB program[8] or fully automatically using ilastik.[56] Tracks were manually curated to remove cells that had died or moved out of frame before the end of movies.

QUANTIFICATION AND STATISTICAL ANALYSIS

Quantification of single-cell p53-Mdm2 protein dynamics

Single-cell p53 and Mdm2 protein levels were quantified according to the p53-mCerulean and Mdm2-SYFP2 signals normalized to nucleus area. Time-series were smoothened using a 1-hour sliding window. To remove the low-frequency background signals, smoothened time-series were subtracted with their polynomial trend lines (second-degree polynomial fit for a time-series of < 72 hours; third-degree polynomial fit for a time-series of > 72 hours, see Figure S12 for the schematics of the single-cell data processing steps). Peaks for p53 and Mdm2 signals were defined using the *findpeaks* function in MATLAB. Valleys were defined as the local minima between two detected peaks. For Figures 1, 2, 3, and 4, we defined pulse amplitude as the polynomial-filtered signal level for each detected peak. For Figures 5, 6, and 7, the polynomial filter was not applied to the p53-Mdm2 time-series due to the extremely low levels of Mdm2 upon *MDM2* knockdown. Instead, we calculated the pulse amplitudes as the signal level at each detected peak, subtracted by that of the preceding valley.

Quantification of p53 and Mdm2 oscillatory periods

For period quantification, the values of peaks and valleys were first normalized to 1 and 0, respectively, in order to enhance the power in their frequency domain. The continuous wavelet transformation of each normalized signal was calculated using a previously developed MATLAB toolbox.[57] The wavelet power spectrum (WPS) was obtained by taking the modulus of the complex-valued wavelet transform. At each time-point, we considered the period component with the highest power to be the signal period. The global WPS was defined as the average of the WPS over time. To quantify inter-peak intervals (IPIs), we calculated the time differences between two consecutive signal peaks. For the bubble plots in Figures 2D and S2D, we applied the same IPI measurement to all time-points between two consecutive peaks. Time-points following the 1:1 Mdm2-to-p53 ratio trendline were defined as having ratios of between 0.5 and 1.5, and those with ratios equal to or above 1.5 belonging to the 2:1 ratio trendline.

Mdm2 pulse skipping identification algorithm

To automatically and rigorously identify Mdm2 pulse skipping events, we developed an algorithm comprising three layers of filters (Figure S2A):

Filter 1 — absence of an Mdm2 peak between two consecutive p53 peaks

After peak finding as described previously, we identified pairs of consecutive p53 peaks with no Mdm2 peak in between them (filter 1, Figure S2A).

Filter 2 — relative integrated rising velocity

Relative integrated rising velocity ($RIVv \rightarrow p$) was defined as the sum of all increases in Mdm2 level (ΔM) relative to that of p53 level (ΔP) during the p53 rising phase. v and p represent the occurrence time of a p53 valley and its subsequent rising peak, respectively. During Mdm2 pulse skipping events, this RIV metric is close to or equal to zero due to the unresponsiveness of Mdm2 to p53 induction. Thus, we used a threshold of RIV as the second filter (filter 2, Figure S2A).

For the RIV analysis, we first matched each pair of p53 and its subquent Mdm2 pulses by applying dynamic time warping to the p53 and Mdm2 time-series. Thereafter, for each pair of p53-Mdm2 pulses, we calculated the relative integrated rising velocity of Mdm2 to p53 as:

$$\mathrm{RIV}_{v \rightarrow p} = \frac{\sum_{t=v}^{p} max\{\Delta M(t), 0\}}{\sum_{t=v}^{p} max\{\Delta P(t), 0\}}$$

To determine the threshold of RIV to filter out oscillatory pulses, we calculated RIV values from all pulses. In the distribution of RIV values of all pulses from the time-series of 406 cells, we observed a local minimum at $\sim 10^{-1.26}$ (Figure S2B). Empirically, this $10^{-1.26}$ value served as an appropriate threshold to distinguish Mdm2 pulse skipping events from oscillatory pulses, thereby allowing us to filter out oscillatory pulses ($RIV > 10^{-1.26}$).

Filter 3 — oscillatory p53 during Mdm2 pulse skipping

To ensure that p53 undergoes oscillation during Mdm2 pulse skipping, we applied Fourier transform to the local p53 dynamics and obtained the period component exhibiting the highest power. We filtered out local p53 periods either too long (> 7.3 hr) or too short (< 2.5 hr) (filter 3, Figure S2A) based on the optimized parameters described below.

To optimize the parameters (peak-finding and p53 period) of this Mdm2 pulse skipping identification algorithm, we sought to establish a ground truth for Mdm2 pulse skipping by manual annotation of standard Mdm2 pulse skipping events (346 skipped events from 100 randomly sampled cells). The principles for annotation follow those described above in the three filters. Next, we identified a parameter set (p53 peak prominence ≥ 4.3; Mdm2 peak prominence ≥ 1.3; p53 peak distance ≥ 2.5 hours; Mdm2 peak distance ≥ 1.5 hours; p53 period > 2.5 hours and < 7.3 hours) that maximizes both precision (proportion of detected skipping events matching standard skipped events, 94.4%) and recall (proportion of standard skipped events detected, 92.5%) to identify Mdm2 pulse skipping events (Figure S2C).

Examining the occurrence of Mdm2 pulse skipping as a random process

First, to determine the time-series of Mdm2 pulse skipping, we considered Mdm2 pulse skipping events as individual point events that could occur at every p53 pulse after NCS treatment (except for the first pulse). Accordingly, we derived a binary time-series of Mdm2 pulse skipping occurrence per p53 pulse for each cell based on the results of the Mdm2 pulse skipping identification algorithm. Next, we amalgamated the single-cell time-series from 406 cells to generate a final time-series for further analysis. The distribution of Mdm2 pulse skipping occurrence was derived from 10,000 randomly selected windows of 30 p53 pulses from the amalgamated Mdm2 pulse skipping time-series and it was compared to a Poisson distribution with a mean value equal to 0.091 skipping events per p53 pulse ($\lambda = 2.72$ per 30 p53 pulses, Figure 2I). The distribution of intervals between two concecutive skipping events in the amalgamated time-series was compared to an exponential function with a mean value equal to $30/\lambda = 11.0$ (Figure 2J).

Quantification of *MDM2* transcriptional intensity

Levels of *MDM2* transcription were quantified according to the signal intensity of nuclear *MDM2*-MS2 foci. First, we applied maximal projection to the mCherry z-stacks, and then performed background subtraction with a rolling ball radius of 50 pixels in Fiji. Cell nuclei were segmented according to the Cy5 channel using StarDist.[55] Overlapping nuclei were separated using the label boundaries function in MorphoLibJ.[58] Using the processed mCherry images and binarized nuclear masks as inputs, we then trained ilastik to distinguish MS2 signal from noise and output the pixel probabilities belonging to MS2 foci.[56] Weighted mCherry intensities were obtained by multiplying mCherry intensities against the probability map. Within each nucleus, MS2 signal was defined as the mean weighted intensity of the nine brightest pixels, normalized to the median nuclear intensity.

Mathematical modeling and stochastic simulations

We developed a bi-allelic mathematical model to quantitatively investigate how formation of the p53-Mdm2 inhibitory complex might give rise to Mdm2 pulse skipping and allelic buffering might impact p53 oscillations. The system is described by the following equations:

$$\frac{d[p]}{dt} = \alpha_p - \lambda_C \cdot \phi \cdot [p] \cdot \sum_{i=1}^{2} [M_i] - \beta_p \cdot [p] \cdot [Q] \qquad \text{(Equation 1)}$$

$$\frac{d[T_i]}{dt} = \alpha_T \cdot (1 - [T_i]) \cdot [p]^2 - \beta_T \cdot [T_i] \quad \text{(Equation 2)}$$

$$\frac{d[m_i]}{dt} = \alpha_m \cdot [T_i] - \gamma_i \cdot \beta_m \cdot [m_i] \quad \text{(Equation 3)}$$

$$\frac{d[M_i]}{dt} = \alpha_M \cdot [m_i] - \lambda_M \cdot \beta_M \cdot [M_i] - \lambda_C \cdot \phi \cdot [p] \cdot [M_i] + \psi \cdot [C_i] \quad \text{(Equation 4)}$$

$$\frac{d[C_i]}{dt} = \lambda_C \cdot \phi \cdot [p] \cdot [M_i] - \psi \cdot [C_i] \quad \text{(Equation 5)}$$

$$\frac{d[q]}{dt} = \alpha_q \cdot [p]^2 - \beta_q \cdot [q] \quad \text{(Equation 6)}$$

$$\frac{d[Q]}{dt} = \alpha_Q \cdot [q] - \beta_Q \cdot [Q] \quad \text{(Equation 7)}$$

We considered a model with one functional p53 protein species (p). Since our experimental results indicate that the expression of *MDM2* mRNA from individual alleles is not always continuous throughout a period of p53 pulse (Figure 4C), we assumed the transcriptional state of the *MDM2* gene (T) is switched on in a p53-dependent manner and is switched off spontaneously, hence reflecting transcriptional bursting.[60,61] Active *MDM2* gene transcription produces *MDM2* mRNA (m), which in turn drives production of Mdm2 protein (M). Mdm2 protein can form the p53-Mdm2 inhibitory complex (C), which reduces levels of functional p53 that can engage transcription, thereby mimicking the transcriptional inhibitory effect (negative feedback loop ii in Figure 3A). Upon complex dissociation, the bound p53 is degraded and Mdm2 is released.

To investigate allelic buffering *in silico*, we introduced two copies of each species of T, m, M, and C, corresponding to the expression from two *MDM2* alleles that regulate p53 independently of each other. We denoted the *MDM2* allele of origin with the subscript i, for $i = 1$ or 2. For simplicity, we assumed all parameters related to those species are the same for both alleles. This design supports the core hypothesis that p53 dynamics are affected by two individual *MDM2* alleles and, based on stochasticity, one of them is by chance not stimulated within a period and thus enables Mdm2 pulse skipping, but expression of the other is sufficient to maintain p53 levels.

We modulated *MDM2* mRNA degradation with the multiplicative factors γ_i, which equal 1 in simulations without *MDM2* allelic knockdown. To simulate single-allele *MDM2* knockdown, γ_2 instead takes the value of 10, *i.e.*, equivalent to a 10-fold increase in the degradation of *MDM2* mRNA from this particular allele. We also associated the complex formation and Mdm2 degradation terms with the multiplicative factors λ_C and λ_M, respectively. These factors take different values within the first 4 hours of the simulations, reflecting the initial response to DNA damage that stabilizes p53 and destabilizes Mdm2 via phosphorylation.[14]

Apart from Mdm2, other transcriptional targets of p53 have been shown previously to negatively regulate p53, such as Wip1, COP1 and Pirh2.[11–13] Therefore, we incorporated a hypothetical species Q to represent other non-Mdm2 negative regulators of p53, with their production of mRNAs (q) itself being driven by p53. This scenario allows for p53 degradation during low expression of both *MDM2* alleles (type IV in Figure 4C). We assumed q mRNA degradation (β_q) displays a similar rate coefficient to that of *MDM2* mRNA (β_m), with Q protein production (α_Q) and degradation (β_Q) having similar rate coefficients to those of Mdm2 protein (α_M and β_M, respectively).

Our simulations generate temporal dynamics for total p53 protein (p^{total}) and Mdm2 protein (M^{total}) in the system, *i.e.*, the sum of unbound and complex-bound proteins:

$$\left[p^{total}\right] = [p] + [C_1] + [C_2]$$

$$\left[M_i^{total}\right] = [M_i] + [C_i]$$

The choice of the model parameters was based on similar values from the literature (see Table S2 for detailed descriptions, values and units of all parameters used).[62–65] Additional criteria were applied in order to recapture the key dynamic features observed experimentally (Figure S6A).

To evaluate the sensitivity of p53 oscillator behavior to perturbations in model parameters, we carried out a sensitivity analysis by varying all parameters two-fold higher and lower, and examined the Mdm2 pulse-skipping frequencies and p53 dynamics after *MDM2* single-allele knockdown. For all perturbations, the Mdm2 pulse-skipping frequency altered within one standard deviation (from 5% to 12%) of the original level (Figure S13A). The p53 amplitude consistently remained higher after *MDM2* single-allele knockdown compared to the control (Figure S13B). There is no difference in p53 period between the *MDM2* single-allele knockdown and control groups (Figure S13C). Overall, both the Mdm2 pulse-skipping frequency and predictions regarding *MDM2* single-allele knockdown are robust to parameter perturbations.

We have also recast the differential equations as individual biochemical reactions to enhance understanding of our model (Table S3).

Implementation of the Gillespie algorithm

We deployed the Gillespie algorithm to simulate the mathematical model via realistic, stochastic implementation.[66] We considered a spatially uniform mixture of N chemical species in a fixed volume, for which the numbers of molecules are denoted $X_1 \ldots X_N$. These chemical species can react through M different reactions, and their propensities are denoted $R_1 \ldots R_M$. At $t = 0$, we considered the initial number of molecules and calculated the propensities of all reactions. Next, we calculated the probability density function (PDF) for the time τ until the next reaction occurred. Within the time interval $[t+\tau, t+\tau+dt]$, the probability that the next reaction $i \in \{1, 2, \ldots, M\}$ occurs is R_i. Thus:

$$P(\tau, i)dt = P_{not}(\tau)^{\text{No reaction in } [t, t+\tau]} \cdot R_i dt^{\text{Reaction } i \text{ occurs}}$$

Given n time windows of infinitesimally small width dt in the time interval $[t, t+\tau]$:

$$P_{not}(\tau) = [P_{not}(dt)]^n = \left(1 - r\frac{\tau}{n}\right)^n = e^{-r\tau}$$

where

$$r = \sum_{i=1}^{M} R_i$$

Therefore, we could generate a random number from the exponential distribution and a random number from the uniform distribution. From the first number, we jumped a step ahead in time τ to the next reaction. With the second number, we selected the reaction according to r. Schematically, the Gillespie algorithm can be described as:

- Pick a random number v_1 from the uniform distribution $U(0,1)$. Using inverse transform sampling, we obtain $\frac{-\ln(v_1)}{r}$, *i.e.*, a random number from the exponential distribution $Exp(r)$. The time until the next reaction is calculated as:

$$\tau = \frac{-\ln(v_1)}{r}$$

- Pick another random number v_2 from the uniform distribution $U(0,1)$. The next reaction to occur is the k^{th} reaction that satisfies:

$$\frac{\sum_{i=1}^{k-1} R_i}{r} < v_2 \leq \frac{\sum_{i=1}^{k} R_i}{r}$$

- Update the system according to the stoichiometry of the chosen reaction.

In this way, the system can be updated and reactions can be adjusted to each time-step. There are 11 different species and a total of 22 reactions in our core system. Each reaction leads to a change in the total number of molecules by ±1, wherein in particular the variable T_i can only take a value of 0 or 1.

Using the Gillespie algorithm to implement realistic stochasticity in our model, we could faithfully recapitulate the dynamics of p53 and Mdm2, as observed experimentally. Specifically, the random occurrence of Mdm2 pulse skipping (as described in Figures 2H–2J and 5B) could only be simulated in the presence of stochasticity, but not in a purely deterministic model. Therefore, our stochastic simulations support that biochemical noise is an important factor controlling the physiological dynamics of p53 and Mdm2.

Detection of Geminin induction

Throughout the experiment, geminin levels were normalized to between 0 and 1, based on the minimum and maximum values found in each individual trace, respectively. We selected G1 cells displaying low Geminin levels upon p53 knockdown, and took the maximum Geminin value in the next 50 hours. These values produced a bimodal distribution, allowing us to set a threshold

(0.2231) to distinguish cells that re-entered S phase (high Geminin) from cells that remained in cell cycle arrest (low Geminin). To visualize Geminin levels (Figure 6I), the mean Geminin level 10-hours prior to p53 knockdown was used for normalization of each individual cell.

Sensitivity analysis

We adapted a previously described method of sensitivity analysis for oscillators.[47] First, we individually perturbed each of the 14 rate parameters (Table S2) two-fold in both directions with respect to their original values. For each parameter value, 500 simulations were then generated. The simulated p53 dynamics were analyzed for amplitude (p53 level at peaks) and period (the period component with the highest power in the global wavelet power spectrum). Due to the stochastic nature of the model, we obtained a distribution of p53 amplitude and period for each parameter perturbation. The sensitivity coefficients (S) were then calculated as:

$${}^{1}S_i^F = \left|Mean\left(F_{i+}\right) - Mean\left(F_{i_0}\right)\right| + \left|Mean\left(F_{i-}\right) - Mean\left(F_{i_0}\right)\right|$$

$${}^{2}S_i^F = \left|STD\left(F_{i+}\right) - STD\left(F_{i_0}\right)\right| + \left|STD\left(F_{i-}\right) - STD\left(F_{i_0}\right)\right|$$

where F is either p53 amplitude or period. The subscripts ($i+$, $i-$, and $i0$) indicate the features given by the increased, decreased, and experimentally derived value of the parameter i, respectively. $Mean(\cdot)$ and $SD(\cdot)$ represent the means and standard deviations of the features over 500 simulations. The sensitivity coefficient quantifies how strong a feature varies in response to a single-parameter perturbation (Figure S8A). The greater the coefficient, the more sensitive the feature. To compare sensitivity between the models in Figure 7A, average sensitivity was calculated as:

$${}^{k}S^F = Mean\left({}^{k}S_i^F\right)$$

where $k = 1$ or 2, representing mean or standard deviation, respectively.

Construction of the p53 oscillatory regime

The rate parameters of *MDM2* transcription (α_m), *MDM2* translation (α_M) and p53-Mdm2 inhibitory complex formation (ϕ) were selected to investigate the plausible biochemical space for a functional p53 oscillator to emerge. We perturbed each parameter between -2 and +2 orders of magnitude at 0.2 order intervals. In total, 9,261 parameter triplets were obtained. We generated 500 simulations for each triplet.

To define functional p53 oscillations, we considered the upper and lower limits of p53 amplitude and period to be two standard deviations away from the mean of the experimental measurements (control cells, Figures 6B–6D), a criterion resembling the known functional p53 oscillations.[23,25] We calculated the values for these limits as follows:

p53 amplitude

To account for differences in p53 amplitude range between experimental and simulated data, we first normalized all experimental p53 amplitudes to the mean of control cells. Two standard deviations above the mean becomes:

$$\frac{Mean(amplitude) + 2 \times SD(amplitude)}{Mean(amplitude)} = 1 + 2 \times CV(amplitude) = 1.8$$

where *CV(amplitude)* stands for the coefficient of variation in the original amplitude distribution. The value 1.8 was therefore used as the upper limit for functional p53 oscillatory amplitude. Similarly, 0.2 was used as the lower limit. We then normalized all simulated p53 amplitudes to the mean of control simulations at their original parameter values. Simulations with normalized p53 amplitudes above 1.8 or below 0.2 were excluded.

p53 period

Two standard deviations above the mean of experimental p53 periods equals 7 hours, thus representing the upper limit for the functional p53 oscillatory period. To exclude short-period fluctuations, we also set a lower limit of 3 hours for functional p53 oscillatory periods. This 3-to-7-hour period range echoes recent findings that the oscillatory p53 period falls within 3.14 to 6.98 hours to enable optimal DNA damage repair.[25]

After defining these criteria, we then searched for the range of parameters that could generate functional p53 oscillations. Since our model incorporates biochemical stochasticity, variations between simulations of identical parameters are possible. Therefore, we considered a parameter triplet to be within the functional p53 oscillatory regime if at least 490 out of 500 simulations (98%) satisfied the defined criteria of p53 dynamics. To ensure the oscillatory regime exists for a sufficiently wide range of parameters, triplets with less than four neighbors in the three-dimensional space of parameters were excluded. The numbers of parameter triplets that could generate functional p53 oscillations were 146 and 563 for the one-allele and two-allele models, respectively.

To visualize the differences in functional p53 oscillatory regimes of the two models, we constructed surfaces from the detected parameter triplets. We first grouped the triplets based on their spatial distance in the parameter space and then used the *alphaShape* function in MATLAB to build concave surfaces to best reflect the shape of the regimes, as shown in Figure 7B.

The half-life of the autocorrelation

To quantify the robustness of p53 oscillations, we adapted a previously described method.[67] First, we applied the *autocorr* function in MATLAB to the p53 oscillations. We then fitted the peaks of this autocorrelation to an exponential decay function ($a + \exp(-bt)$) using MATLAB's *fitnlm* function. From the fitted parameters, we calculated the half-life of the autocorrelation as a measurement of the robustness of oscillations. A longer half-life indicates more robust, noise-resistant p53 oscillations.

Statistical analysis

The statistical tests performed are stated in the figure legends. The biomodality in p53 and Mdm2 period was determined by the Cheng and Hall test.[68] For all comparisons of amplitudes and periods, both Cohen's d and non-parametric tests are employed. The statistical assessment for Cohen's d effect size is included in Table S4. Sample size and other details are given either in the figure legends or summarized in Table S5.